Chemical and Physical Properties

of Variable Stars in

Globular Clusters

A thesis submitted to The University of Manchester for the degree of

Master of Science by Research

in the Faculty of Engineering and Physical Sciences

2015

Kyle Warrington

School of Physics and Astronomy

Contents

CONTENTS

CONTENTS

PROPERTIES OF VARIABLE STARS IN GCS

List of Figures

LIST OF FIGURES

PROPERTIES OF VARIABLE STARS IN GCS

List of Tables

The University of Manchester

ABSTRACT OF THESIS submitted by Kyle Warrington

for the Degree of Master of Science by Research and entitled

Chemical and Physical Properties of Variable Stars in Globular Clusters. 2015.

A study of 14 stars in seven different globular clusters has been undertaken. Ten of these stars are variable stars, while the four stars from NGC 7099 were used because they are near the RGB tip. Stellar parameters were determined by measuring the equivalent widths of absorption lines in the stellar spectra as well as other element abundances. The stellar parameters measured are: effective temperature (T_{eff}), surface gravity ($\log(g)$), metallicity ([Fe/H]) and the microturbulent velocity (v_{t}). This was done using MOOG (Sneden 1973) and Kurucz (1981) model atmospheres. MOOG `synth` was used for the spectral lines of O, Na, Mg, Al and Rb that were heavily blended or sensitive to other elemental abundances.

The resulting stellar parameters have shown NGC 7099 4 to be a foreground star. Using available period data and spectral energy distribution fits, the remaining 13 stars were classified into five post-AGB stars and eight RGB/AGB stars.

The "generation" for each star was determined using Na/O and Mg/Al plots. Three of the post-AGB stars are of particular interest. NGC 7492 V4 is a primordial star with a normal turnoff point at the tip of the AGB with high luminosity. It can be compared with NGC 7089 V5 and V6: potentially extreme stars and thus second-generation. V5 and V6 are likely to be He-rich due to having a much lower luminosity turnoff point from the AGB. This He-enrichment comes from being second-generation stars.

Two stars had measurable rubidium lines that came out with the expected near-solar [Rb/Fe] ratio. Three stars with upper limits for Rb were found to be Rb-deficient.

Declaration

I declare that no portion of the work referred to in the thesis has been submitted in support of an application for another degree or qualification of this or any other university or other institute of learning.

Copyright Statement

(i) The author of this thesis (including any appendices and/or schedules to this thesis) owns certain copyright or related rights in it (the "Copyright") and s/he has given The University of Manchester certain rights to use such Copyright, including for administrative purposes.

(ii) Copies of this thesis, either in full or in extracts and whether in hard or electronic copy, may be made only in accordance with the Copyright, Designs and Patents Act 1988 (as amended) and regulations issued under it or, where appropriate, in accordance with licensing agreements which the University has from time to time. This page must form part of any such copies made.

(iii) The ownership of certain Copyright, patents, designs, trade marks and other intellectual property (the "Intellectual Property") and any reproductions of copyright works in the thesis, for example graphs and tables ("Reproductions"), which may be described in this thesis, may not be owned by the author and may be owned by third parties. Such Intellectual Property and Reproductions cannot and must not be made available for use without the prior written permission of the owner(s) of the relevant Intellectual Property and/or Reproductions.

(iv) Further information on the conditions under which disclosure, publication and commercialisation of this thesis, the Copyright and any Intellectual Property and/or Reproductions described in it may take place is available in the University IP Policy (see http://www.campus.manchester.ac.uk/medialibrary/policies/intellectual-property.pdf), in any relevant Thesis restriction declarations deposited in the University Library, The University Library's regulations (see http://www.manchester.ac.uk/library/aboutus/regulations) and in The University's policy on presentation of Theses.

Acknowledgements

I would like to thank my supervisor, Iain McDonald, for all his help and support throughout this year.

I would also like to thank Carmel Roche and Paulo Freitas for all their support when writing my thesis.

This thesis was typeset with LaTeX.

The Author

The author graduated from Keele University in 2014 with a BSc in Astrophysics. Since then he has been studying for an MSc by Research in Astronomy and Astrophysics at the Jodrell Bank Centre for Astrophysics. The results of this research are presented in this thesis.

List of Abbreviations and Symbols

The following abbreviations and symbols are used throughout this thesis:

AGB − Asymptotic Giant Branch

H–R diagram − Hertzsprung–Russell diagram

HB − Horizontal Branch

HBB − Hot Bottom Burning

$L_\odot$ − Solar Luminosity

LPV − Long Period Variable

$M_\odot$ − Solar Mass

MS − Main Sequence

RGB − Red Giant Branch

SED − Spectral Energy Distribution

TP-AGB − Thermally Pulsating Asymptotic Giant Branch

MIKE − Magellan Inamori Kyocera Echelle

ISM − Interstellar Medium

SAGB - Super-AGB

E.P. - Excitation Potential

LTE - Local Thermodynamic Equilibrium

1

Introduction

1.1 Motivation

Chemical enrichment of the Universe first started after the Big Bang. The first stars are known as Population III stars and were created from the primordial medium. These stars are thought to have been very massive with typical masses $\gtrsim 100 M_\odot$, therefore, the stars quickly went through their evolutionary lifetimes and created metals (elements other than hydrogen and helium; Bromm and Larson 2004). The metals were then ejected into the interstellar medium by supernovae. To discover more about Population III stars we have to look at the oldest observable stars, those known as Population II stars (Frebel 2010a). Studying the chemical composition of these stars and their metal abundances will provide information on the previous generation.

Globular clusters contain many of the oldest stars in the Universe, providing some of the best areas to study, due to the amount of Population II stars readily available and their being comparatively nearby.

Variable AGB and post-AGB stars in Globular Clusters show evidence of chemical modification of their surfaces during their evolution, which can be found by comparing to less-evolved stars by the elements formed. Establishing the abundances of elements throughout the cluster also traces the stars that contributed to the enrichment before

the cluster formed. The fundamental parameters and chemical composition can also be accurately determined to see how chemistry affects the AGB tip, such as helium enrichment (Campbell et al. 2013).

1.2 Definitions

1.2.1 Abundance

The main form in which atomic abundance that will be expressed in this thesis is the 'square-bracket' notation. However, the 'ϵ' notation will also be used.

In the 'square-bracket' notation, the abundance is expressed relative to that of the Sun. Considering iron and hydrogen, Fe and H, we have:

$$[\text{Fe/H}] = \log_{10}(N_{Fe}/N_H)_{star} - \log_{10}(N_{Fe}/N_H)_{\odot}, \tag{1.1}$$

where N_{Fe} and N_H represent the number of atoms of Fe and H elements respectively, and can be changed for any element. The quantity [Fe/H] is often used as an easily observed approximation for metallicity, where metallicity is the proportion of chemical elements in a star other than hydrogen and helium.

In the 'ϵ' notation, the abundance of an element is expressed relative to 10^{12} hydrogen atoms. Thus, using an element A:

$$\log_{10} \epsilon(A) = \log_{10}(N_A/N_H) + 12. \tag{1.2}$$

1.2.2 Stellar Populations

Population III stars formed from primordial gas, thus were hypothetically metal free. The first elements created shortly after the Big Bang were ^{1}H, ^{4}He with trace amounts of ^{2}H, ^{3}H, ^{3}He and ^{7}Li (Frebel 2010a). Undergoing supernovae, these stars ejected newly synthesized metals into the interstellar medium (ISM). From their ejecta, Population II stars were created. These are now observable as old, metal-poor stars, found

mostly in the 'haloes' of large galaxies, dwarf spheroidal galaxies and globular clusters (Beers and Christlieb 2005). Population I stars are younger, metal-rich stars found in the disks of galaxies. An example of a Population I star would be our Sun.

The definition of what metal-poor actually means is variable, Beers and Christlieb (2005) propose definitions for stars with differing metallicity and is an attempt to classify what metal-poor stars are. They define stars with [Fe/H] of -1.0 to be metal-poor. Stars with [Fe/H] < -2.0 are known to be very metal-poor with this continuing down to [Fe/H] < -5.0. Frebel et al. (2005) have observed a star with a metallicity of [Fe/H] $= -5.6$. These final stars are known as hyper-metal-poor and are often used in stellar archeology (see Frebel 2010b, for a review of stellar archeology). These stars are the oldest observable stars and record the heavy element abundances produced by first-generation stars. By measuring these abundances and comparing with predictions from stellar evolution models, more information can be gathered on the previous generation, including their formation and evolution.

1.3 Measuring Stellar Abundances

This section will cover the programs and methods that will be used to find metal-poor stars and then learn more about their fundamental properties that will be used to trace the evolution of the first stars.

1.3.1 Background to Spectroscopy

Spectroscopy is one of the fundamental tools at an astronomer's disposal. It allows the determination of stars' chemical compositions, physical properties and radial velocities. Using these properties, and by analysis of spectral features, models can be constrained of chemical enrichment in galaxies and the evolution of the Universe.

The most common form of a spectrum that can be seen is the light from the Sun that has been dispersed to show a rainbow. However, it was Isaac Newton (1643-1727)

who first showed that sunlight could be dispersed into a continuous series of colours using a prism. This was extended on further by Joseph van Fraunhofer (1787-1826) who discovered and characterized the dark bands evident when the Sun's spectrum is sufficiently dispersed. The explanation of these dark bands was not understood until the work of Gustav Kirchhoff (1824-1887) and Robert Bunsen (1811-1899), who proposed that they were due to the selective absorption of a continuous spectrum produced by the hot interior of the sun by cooler gases at the surface. The spectra of other stars were first observed visually by Fraunhofer and Angelo Secchi (1818-1878), either of whom may be credited with having founded the science of astronomical spectroscopy.

1.3.2   Measuring Spectra

Atmospheric windows are a range of electromagnetic wavelengths to which the Earth's atmosphere is largely or partially transparent. All spectral regions are affected to some extent by absorption in the atmosphere but there are two nearly transparent ranges, the optical window and the radio window, and several narrow, partially transparent infrared windows.

A spectrograph separates light into a frequency spectrum and records the signal. An Echelle spectrograph uses a plane grating at high angles of incidence and diffraction, or equivalently at very high orders, to take advantage of the consequent high resolution and dispersion. It is used over a smaller range of angles and can therefore be blazed with a well shaped groove to be more efficient throughout a very wide range of wavelengths. To individually resolve all the wavelengths the Echelle spectrograph must use a second dispersion element of lower dispersion to be able to resolve the different free spectral ranges. This setup is used in the Magellan Inamori Kyocera Echelle (MIKE) spectrograph (Bernstein et al. 2003) which is a double echelle spectrograph on the 6.5m Magellan Clay telescope at Las Campanas Observatory. In standard observing mode, the blue (320-480 nm) and red (440-1000 nm) channels are used simultaneously to obtain spectra over the full wavelength range, with only a few gaps in wavelength

coverage at the reddest orders.

The spectral resolution of a spectrograph, or, more generally, of a frequency spectrum, is a measure of its ability to resolve features in the electromagnetic spectrum. $\Delta\lambda$ is the smallest difference in wavelengths that can be distinguished at a wavelength, λ, and is closely related to the resolving power of the spectrograph, defined as:

$$R = \lambda/\Delta\lambda \tag{1.3}$$

MIKE has a resolving power ranging from 19,000 to 71,000, depending on if it is using the red or blue channel and the size of the slit (Bernstein et al. 2003).

A spectral line is a dark or bright line in an otherwise uniform and continuous spectrum, resulting from a deficiency or excess of photons in a narrow frequency range, compared with the nearby frequencies. They can either be absorption lines or emission lines. Absorption lines are dark lines in a broad-spectrum that are produced when a cold gas is between a broad spectrum photon source and the detector. The incident photon is absorbed by a source and then re-emitted in a random direction. Or, by contrast, if the detector sees photons emitted directly from a (hot) glowing gas, it will observe photons emitted in a narrow frequency range by quantum emission processes in atoms in the gas, and this results in an emission line (Murdin 2000).

The equivalent widths of spectral lines (see Figure 1.1) are a measure of the area of the line on a plot of intensity versus wavelength. They are found by forming a rectangle with a height equal to that of continuum emission, and finding the width such that the area of the rectangle is equal to the area in the spectral line. It is a measure of the strength of spectral features and is defined as:

$$W = \int \frac{F_c - F_\lambda}{F_c} d\lambda, \tag{1.4}$$

where F_c is the continuum intensity on either side of the spectral feature, while F_λ represents the intensity across the entire wavelength of interest.

Using the equivalent width, a curve of growth can be obtained which is a graph
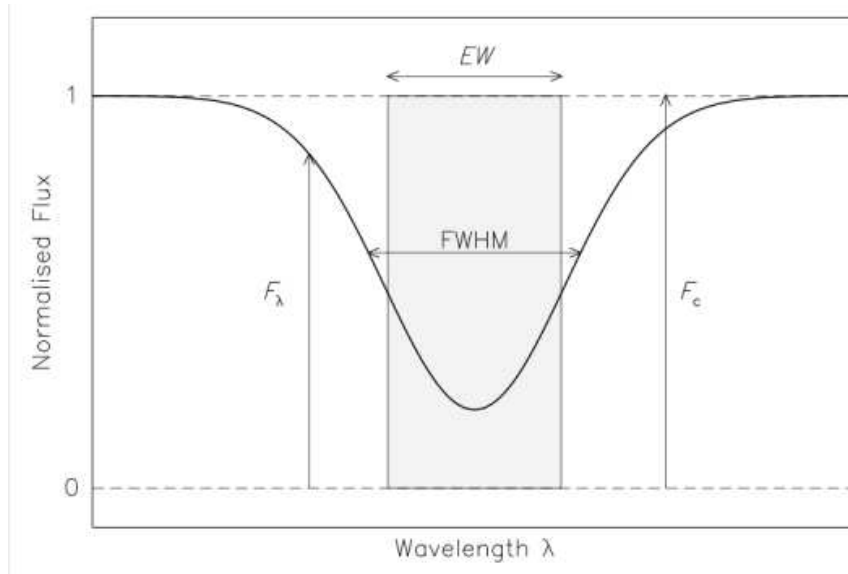
Figure 1.1: The equivalent width of an absorption line is defined as the width of the rectangle that has an area equal to the area in the spectral line, as illustrated in grey. Adapted from Figure 9.18 of Carroll and Ostlie (1996).

showing how the equivalent width of an absorption line, or the radiance of an emission line, increases with the number of atoms producing the line. Using this graph and with knowledge of the physical conditions in the gas, the abundance of the chemical can be found.

A popular code that is used to determine the chemical composition of a star is MOOG[1] (Sneden 1973). MOOG is a Fortran code that performs a variety of spectral line analysis and spectrum synthesis tasks under the assumption of local thermodynamic equilibrium. MOOG uses a model photosphere based on the Kurucz stellar models (Kurucz 1981) together with a list of atomic or molecular transitions to generate an emergent spectrum by solving the equations of radiative transfer. A standard MOOG running option called `abfind` models equivalent widths for specific parameters. These can be compared to observations to identify the conditions in the stellar photosphere and elemental abundances.

Spectral synthesis programs often use previously generated model photospheres to

---

[1]http://www.as.utexas.edu/ chris/moog.html

describe the physical conditions (temperature, pressure, etc...) through which photons must travel to escape the stellar atmosphere. Together with a list of absorption lines and an elemental abundance table, spectral synthesis programs generate synthetic spectra. By comparing these synthetic spectra to observed spectra of distant stars, astronomers can determine the properties (temperature, surface gravity, chemical composition, with effort, age, etc...) of these stars. Another standard MOOG running option is called `synth` that can be used to compute a plot. Following this, abundances can be deduced by fitting the synthetic spectrum to the observed spectrum through modifying abundances of single or multiple elements to line up the spectra. This can be done over the whole spectrum on well known lines.

1.4 Evolution of Low-Mass Stars

1.4.1 Stellar Evolution of a 0.8M$_\odot$ Star: Main Sequence to White Dwarf

Stars are formed from dense molecular clouds that are typically composed of mostly hydrogen and helium. Figure 1.2 shows the evolution of a Sun-like star which is sufficiently similar for this discussion to a 0.8M$_\odot$ star. The figure also includes the time-scales involved for each phase of evolution for said star along with the main events that happen during that phase.

From the beginning of its life, a Sun-like star burns hydrogen in its core to form helium via the proton-proton chain and releases energy (Iben 1967). Most stars spend the majority of their lifetimes on the main sequence, with 0.8M$_\odot$ stars spending roughly 10-15 Gyrs here (Dotter et al. 2007). During hydrogen burning, an inert helium core is formed. Hydrogen burning carries on until hydrogen in the core is exhausted and the star moves onto the Red Giant Branch (RGB). The energy production then moves into the hydrogen shell. This causes the equilibrium between the outward pressure and gravity to be broken.
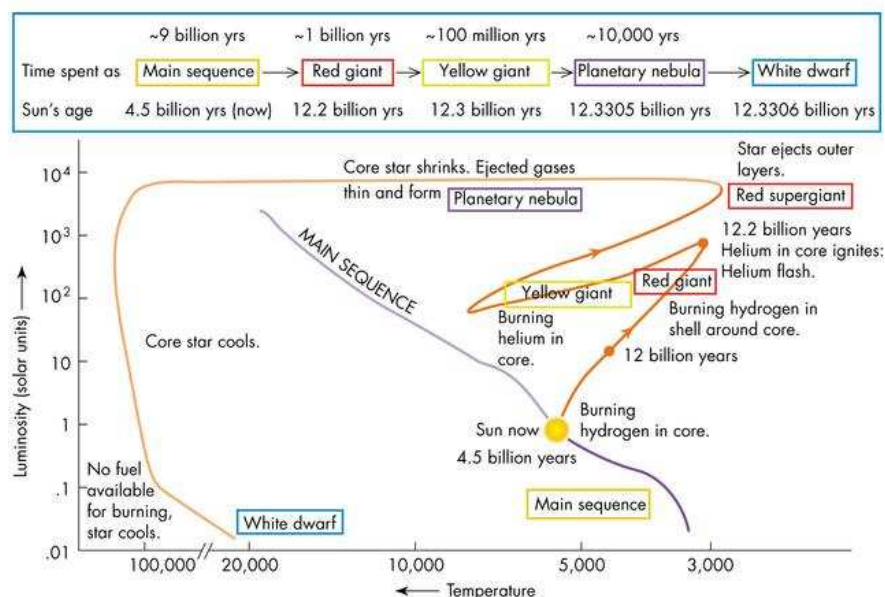
Figure 1.2: Hertzsprung-Russell diagram showing the evolution of a Sun-like star including time-scales and main events for each phase. $0.8M_\odot$ is slightly lighter than the Sun however the evolution is qualitatively the same. This picture was taken from http://www.profjohn.com/courses/ast1004/starlives/starlives.htm.

Red Giant Branch

Once on the RGB the core begins to contract. The contraction causes the inert helium core to increase in temperature which then heats up the surrounding hydrogen shell, which increases the rate of burning in the hydrogen shell. The helium core will continue to contract until it is dense enough to be supported by electron degeneracy pressure. The gravity the core exerts compresses the hydrogen shell causing the hydrogen to burn faster. This causes more energy to be created so that the star becomes more luminous and the envelope expands. Due to this expansion, the outer convective envelope also expands inward and penetrates into the CN-cycle-processed interior regions (Gratton et al. 2000). The products of hydrogen fusion, ^{12}C, ^{13}C, ^{14}N, ^{16}O, ^{17}O, ^{18}O, ^{20}Ne and ^{22}Ne, are then brought to the surface during this stage, called first dredge-up (Boothroyd and Sackmann 1999).

The ensuing mixing episode is predicted (Iben 1964) to alter the surface light element abundances of the star. For stars of solar mass and luminosity there should be a moderate depletion of ^{12}C. This lowers the ^{12}C/^{13}C ratio from the original value (assumed to be nearly solar, $\sim$ 70; Bethe 1939) down to about 20-30, and increasing ^{14}N by a corresponding amount (Iben and Renzini 1984). First dredge-up is expected to be less efficient in metal-poor stars (Vandenberg and Smith 1988; Charbonnel 1994): using a stellar model with metallicity of 0.001 and $0.8M_{\odot}$, the changes in C and N abundances are very small, with the ^{12}C/^{13}C ratio expected to remain > 30 (Gratton et al. 2000).

However, first dredge-up cannot justify inhomogeneities found in carbon abundances for RGB stars in metal-poor clusters. An example of this was found by Bell et al. (1979) in M92 where the carbon abundance was a decreasing function of luminosity. This trend was confirmed by Suntzeff (1981) for M3 and M13. This implies that there must be some other form of mixing, other than the first dredge-up, within RGB stars. This mixing is called deep mixing or extra mixing.

This mixing must be sufficiently slow to carry a considerable volume of ^{13}C to the surface so that the ^{12}C/^{13}C ratio decreases from 25-30 at the first dredge-up, down to 12-15 (in Population I stars) or to 4-8 (in Population II red giants). [O/Fe] ratios are affected by deep mixing, generally by decreasing [O/Fe] and increasing [Na/Fe] especially in He-rich, Na-rich and O-poor globular clusters (Johnson and Pilachowski 2012). Extra / deep mixing is a continuous process, operating mostly on the uppermost RGB (see Johnson and Pilachowski 2012, on M13).

Throughout the RGB phase, the core of the star continues to heat up. However, for a star of an initial mass of $0.8M_{\odot}$ the helium core still is not hot enough to ignite and has been degenerate since the star left the main sequence. The degeneracy pressure increases and eventually becomes sufficient to prevent further collapse of the most central material. However, the star still contracts, increasing the temperature. Once the temperature reaches approximately 10^8K then helium ignition occurs and the star moves off the RGB. This runaway fusion of helium in the core of low mass stars of

less than about 2.3M$_\odot$ is termed the helium flash (Stancliffe et al. 2005). This happens due to the degenerate helium core, meaning it is supported against gravity by quantum mechanical pressure rather than thermal pressure. Thus an increase in the temperature of the material undergoing fusion does not act to expand the material and by doing so cool it, and there is no regulation of the rate of fusion. The very high density also speeds up the fusion rate. The subsequent runaway nuclear reaction emits energy at a rate comparable to the whole Milky Way, but only for a few seconds. In the case of normal low mass stars, the energy is absorbed by the star and not visible from outside. The process ends when the material is heated to the point where thermal pressure again becomes dominant, and the material then expands and cools. The helium flash, undetected by observation, is described by astrophysical models (Deupree and Wallace 1987).

Horizontal Branch

Once the helium flash has subsided, the star returns to a normal, non-degenerate state. The star undergoes helium burning inside the core through the triple-α process which involves three helium atoms to form a carbon atom and, in some cases, can go even further to form oxygen. The star then moves onto the horizontal branch (HB). The helium core flash causes substantial changes in stellar structure, resulting in an overall reduction in luminosity, some contraction of the stellar envelope, and surfaces reaching higher temperatures. HB stars are powered by helium fusion in the core and by hydrogen fusion in a shell surrounding the core (Catelan 2009). The envelope mass of the star dictates its temperature on the HB. The envelope mass is determined by a combination of the star's initial mass, the mass-loss history on the RGB and the helium enrichment (which shortens its lifetime) (Catelan 2009).

Barnard (1900) was the first to detect the presence of (blue) horizontal branch stars in globular clusters. The term horizontal branch appears to have been coined by ten Bruggencate (1927). He noticed this when plotting the colour-magnitude data obtained by Shapley (1915) in the his study of NGC 5272 (M3). Of course, with the

development of nuclear astrophysics and the establishment of modern stellar evolution theory still several years away, it was not until three decades later that Hoyle and Schwarzschild (1955) first correctly identified HB stars as the progeny of low-mass RGB stars, burning helium in their core and hydrogen in a shell around the core.

Asymptotic Giant Branch

Once the helium core is exhausted, the core contracts and enters the Asymptotic Giant Branch (AGB). The core of this star is now formed by inert carbon for stars $\lesssim 5M_\odot$, surrounded by a helium burning shell and a hydrogen burning shell (Iben and Renzini 1983). Ignition in the core of the star, to fuse carbon and oxygen into heavier elements, is only possible in massive stars of a mass $\gtrsim 8M_\odot$.

Eventually the helium shell survives on the ashes of the hydrogen burning shell. However, there is sufficiently little fuel that nuclear burning of helium is quenched. It then becomes a thermally pulsing AGB (TP-AGB). During this stage, third dredge-up can occur, which mixes the ashes of the helium burning shell with the convective envelope enhancing the surface abundance of carbon (Iben and Renzini 1983). Now the star derives its energy from fusion of hydrogen in a thin shell, which restricts the inner helium shell to a very thin layer and prevents it fusing stably (Pols et al. 2001). Over periods of 10^4 to 10^5 years, helium from the hydrogen shell burning builds up and eventually the helium shell ignites explosively, a process known as a helium shell flash (Pols et al. 2001). The shell flash causes the star to expand and cool which shuts off the hydrogen shell burning. This allows strong convection from the region between the two shells, known as the intershell region, so that the elements mix into the outer envelope. The convective mixing is a two-stage process by which convection reaches across the helium burning shell to dredge material from the core to the intershell region, followed by the convective envelope penetrating through the inert hydrogen burning core into the intershell region to mix that material to the stellar surface (Herwig 2005). As the helium burning reaches the base of the hydrogen shell, the hydrogen is re-ignited and the cycle starts again causing more helium flashes which are the thermal pulses.

Material is ejected through stellar winds and the C-O core and envelope separate. The mass-loss mechanism that removes the stellar envelope depends on the process that initiates the outflow (Elitzur et al. 2003). The majority of the mass loss occurs on the RGB through electro-magneto-acoustic processes, likely via chromospheric heating (see McDonald and Zijlstra 2015b; Dupree et al. 1984; Schröder and Cuntz 2005). Another mechanism, based on observations and theoretical studies, is stellar pulsations (Wood 1979; Bowen 1988; Winters et al. 2000). This process only effects the upper AGB and is a small part of the mass loss for 0.8 $M_\odot$ stars.

The circumstellar envelope is the part of the star above the photosphere which has a roughly spherical shape and usually most is gravitationally bound to the star core. Here the first condensates are either oxides or carbides depending on whether the star is carbon-rich or oxygen-rich (Habing 1996). The stellar winds from AGB stars are sites of cosmic dust formation, and are believed to be a major production site of dust in the Universe (Schneider et al. 2014). After these stars have lost nearly all of their envelopes, and only the core regions remain, they evolve further into short-lived post-AGB stars. These stars have ended their AGB evolution with a phase of very strong mass loss ($10^{-7} - 10^{-4} M_\odot yr^{-1}$). They have evolved on a fast track to hotter effective temperatures at roughly constant luminosity, but are not yet hot enough to ionise the circumstellar material and to emerge as a planetary nebula, prior to cooling down as a white dwarf (van Winckel 2003). The final fates of the AGB envelopes are represented by planetary nebulae. However, most stars in globular clusters are not massive enough to create planetary nebulae except in a close binary (Jacoby et al. 2014). They evolve through the post-AGB phase so slowly that the envelope is dispersed before the central star is hot enough to ionise it.

From the loss of the envelope, the remnant C-O core no longer has any viable nuclear reactions to create energy. This causes the core to radiate its remaining energy and cool down to end its life as a white dwarf. The white dwarf is degenerate and only supported by electron degeneracy pressure.

1.5 Evolution of High-Mass Stars

1.5.1 Stellar Evolution of a 5-10 $M_\odot$ Star

More massive stars will go through their stellar evolution a lot quicker than the star from the previous chapter. Massive stars have a lot more hydrogen available for nuclear reactions allowing more reactions to take place simultaneously, making the star more luminous. With more fusion taking place, more energy is being released from the core as both thermal energy and radiation. The increase in temperature within the core causes the hydrogen molecules to move faster and collide with higher energies that will increase the chance of further reactions to occur. This process continues until the hydrogen in the core is used up and the star moves off the main sequence. However, these stars still follow a similar evolution as defined before.

Once these stars reach the AGB phase there is another stage that can only be undergone by the most massive AGB stars (6-8$M_\odot$) (Habing 1996). This stage is known as Super-AGB (SAGB) and also requires off-centre ignition of carbon to form a degenerate oxygen and neon core (Jones et al. 2013). Owing to their massive oxygen-neon core, SAGB stars suffer weak thermal pulses, have very short interpulse periods and develop very high temperatures at the base of their convective envelope (up to 1.4 x 10^8 K), leading to very efficient hot bottom burning (Siess 2010). Hot bottom burning is where proton-capture nucleosynthesis happens at the base of the outer envelope that favours the conversion of C to N by the CN-cycle and reconversion of the C-rich to an O-rich atmosphere (García-Hernández et al. 2013). SAGB stars are consequently manufacturers of ^{4}He, ^{13}C, and ^{14}N. They are also able to inject significant amounts of ^{7}Li, ^{17}O, ^{25}Mg, and ^{26,27}Al into the ISM (Siess 2010).

Following the SAGB phase there are two different remnant pathways these stars can go, type II supernovae and planetary nebulae. The type II supernovae result from the rapid collapse and violent explosion of massive stars and usually occur for stars of M > 8$M_\odot$. Figure 1.3 shows a typical composition for the late stages of evolution for a high mass star. It contains an inert iron-nickel core with nuclear burning shells.
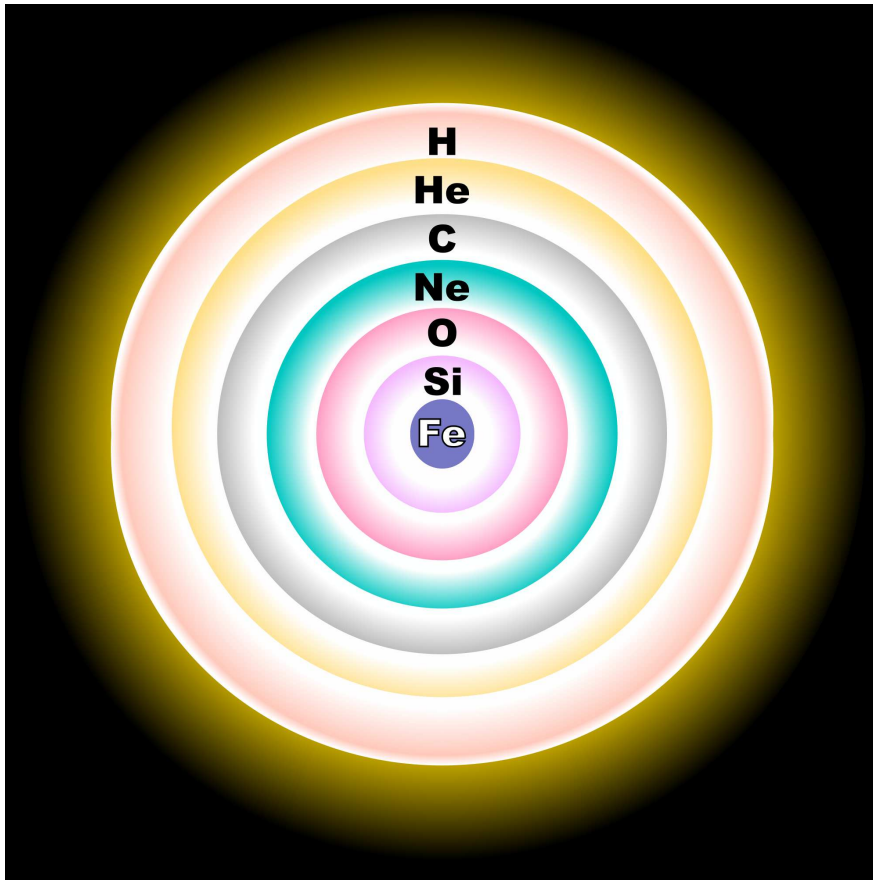
Figure 1.3: This shows the typical chemical composition of a high mass star close to the end of its lifetime. This picture was taken from http://upload.wikimedia.org/wikipedia/commons/thumb/3/37/Evolved_star_fusion_shells.svg/2000px-Evolved_star_fusion_shells.svg.png.

Once the core exceeds the Chandrasekhar limit of $1.4M_\odot$ then electron degeneracy pressure can no longer sustain an equilibrium inside the core and it rapidly implodes. During the implosion, which takes place within seconds, the temperature dramatically increases. The collapse is halted by neutron degeneracy and the implosion rebounds and bounces outwards. This causes a shock wave of sufficient energy to accelerate surrounding stellar material. Due to the extreme temperatures in the shock wave and available energy, elements heavier than iron are formed and carried along with the shock wave. For this mass range the star will end it's life as a neutron star or a black hole.

At the end of the SAGB phase for lower-mass stars, the star's outer layers are expelled by strong stellar winds. After most of the envelope has been dissipated, the exposed hot, luminous core emits ultraviolet radiation to ionise the ejected outer layers of the star. Planetary nebulae therefore return material to the ISM that were the product of nucleosynthesis, including carbon, nitrogen, oxygen and neon.

1.6 Abundances in Globular Clusters

1.6.1 Overview

A globular cluster is a spherical collection of stars that orbits the galactic centre as a satellite. Globular clusters are very tightly bound by gravity, which gives them their spherical shapes and relatively high stellar densities toward their centres. They contain considerably more stars and are much older than the less dense galactic, or open clusters, which are found in the disk. They are conglomerations of roughly 10^4 to 10^6 stars (Benacquista 2002) which show a strong, but variable degree of central condensation. Globular clusters contain some of the oldest stars in the galaxy which were created from the first generation of stars. It is clear that globular clusters are significantly different from dwarf galaxies and were formed as part of the star formation of the parent galaxy rather than as a separate galaxy (Bellazzini 2015). Dwarf galaxies were also formed with and contain dark matter, however, a globular cluster does not contain any dark matter (Gnedin 2003).

Evidence suggests that stars within most or all globular clusters have roughly the same age. The absolute ages are difficult to determine: estimated ages for Galactic globular clusters are typically 10-15 Gyr (Ashman and Zepf 1998; Jimenez 1998). This means that they contain the oldest and first stars formed in the Universe (which has an age roughly 13.73 ± 0.12 Gyr; Hinshaw et al. 2009). Globular clusters are generally comprised of very metal-poor stars, metallicities range from [Fe/H]= -2.3 to solar metallicity, though typically [Fe/H] $\approx -1.4 \pm 0.6$ (Harris 1996). They have similar

ages of stars to the types of stars found in the bulge of a spiral galaxy but confined to a volume usually less than a few million cubic parsecs. Globular clusters are also largely free of interstellar gas and dust, thought to be cleared out by thermal pressure and perhaps pressure stripping by hot halo gas (McDonald and Zijlstra 2015a).

1.6.2   The *r*- and *s*-Processes

The enrichment of globular clusters came from previous generations of stars. For the oldest cluster stars this enrichment would have come from Pop. III stars formed by the primordial medium following the Big Bang. Most of the heavier elements (Z > 30) are produced either by slow or rapid neutron-capture reactions (the so-called s- and r-processes), where both processes occur in different physical conditions and are thus likely to happen in different astrophysical sites (James et al. 2004).

The creation of n-capture elements is easily divided into two extreme cases of neutron intake and β-decay timescales being the *r*- and *s*-processes (Burbidge et al. 1957; Cameron 1957). if $\tau_n >> \tau_\beta$ then unstable nuclei will have time to execute all β-decays between successive neutron captures, and element production proceeds along the "valley of β stability" (Sneden et al. 2010). This relatively slow nucleosynthesis mechanism is called the *s*-process and usually takes place at low neutron densities. It is normally a by-product of inactive He-burning, most easily accomplished during the AGB phase of low-intermediate mass stars (Sneden et al. 2010). At the opposite extreme, if if $\tau_n << \tau_\beta$ then nuclei are (for a few seconds at most) overwhelmed with neutrons. When the flood of neutrons stops, β-decays occur until stability is reached. This rapid-burst mechanism is called the *r*-process. This process is usually associated with the explosive deaths of high-mass stars (supernovae).

In the build-up to progressively heavier elements via the *s*-process, bottlenecks form around specific numbers of neutrons (e.g., 50, 82, 126) which form nuclear structures that are more stable against neutron capture than their neighbours (Busso et al. 1999). This causes three major peaks to develop: a light *s*-peak (Sr, Y, Zr), a heavy

s-peak (Ba, La, Ce), and a peak at Pb, with a light peak forming first and the heavier peaks forming later with increasing neutron exposure (Shingles et al. 2014). Shingles et al. (2014) investigated the globular clusters M4 (NGC 6121) and M22 (NGC 6656) and found that both have produced *s*-process elements. They found that M4 is enriched mostly with light *s*-peak elements while M22 is more weighted towards heavy *s*-peak elements and Pb.

As for the *r*-process, the sole indicator for this process in globular clusters is usually from Eu measurements (Yong et al. 2010). However, the *r*-process requires a rapid intake of neutrons which mainly comes from supernovae which do not happen in globular clusters. Honda et al. (2012) found in their investigation of three similar metal-poor globular clusters (M15, M30 and M92) that there was a star-to-star scatter of Eu abundance ratios and were homogeneously enriched in lighter neutron-capture elements such as those found from the *s*-process.

1.6.3   Multiple Populations in Globular Clusters

Sandage and Wallerstein (1960) noticed that the distribution with colour/temperature of stars on the HB of globular clusters is roughly correlated with their metal content. A few years later, this observation was explained by the first successful models of HB stars describing the effect of metal content on the efficiency of H-shell burning in low mass stars where He is burning in the core (Faulkner 1966). However, soon after this important theoretical achievement, van den Bergh (1967) and Sandage and Wildey (1967) pointed out that the correlation between colour/temperature and metallicity had several exceptions, a difficulty that has become known as the second parameter problem. This problem is difficult to solve, one of the more important reasons behind this is that there is most likely more than a single second parameter (Gratton et al. 2010a).

Many observations show that globular clusters are composed of (at least) two distinct stellar populations. Deep photometric studies have revealed multiple giant branches and main sequences in globular clusters. In ω Cen a blue main sequence has

been discovered (Bedin et al. 2004) that is thought to be related to a high He content (Piotto et al. 2005; Villanova et al. 2007), which shifts the effective temperatures towards hotter values. He-rich stars have also been proposed to explain the morphology of extended HBs seen in many globular clusters (see, e.g., Caloi and D'Antona 2005). For a given stellar mass, He-rich stars evolve faster on the main sequence due to their lower initial H-content and to their higher luminosity. This also leads their progeny on the HB to be less massive than that of He-poor stars (Norris et al. 1981), giving them higher temperatures. Once these stars reach the post-AGB phase they often have lower luminosities. This is due to their faster evolution as they have started out with lower mass than helium-normal post-AGB stars.

Helium abundances are hard to determine as no He lines are visible in cool stars (Cuntz and Luttermoser 1990), so it is much easier to determine the abundances of other elements, including Na and O. It is very clear that anticorrelations between oxygen and sodium abundances persist in almost all globular clusters studied using high-resolution spectroscopy (Carretta et al. 2009b). The physical processes involved in the Na-O anticorrelation appear to be certain; oxygen is depleted by the CNO cycle while sodium is enriched from the ^{22}Ne(p, γ) ^{23}Na reaction in the hydrogen-burning shells of evolved stars (Lee 2010). A scenario for Na-O anticorrelation requires at least two generations of star formation in globular clusters. Chemical pollution from the first generation of intermediate-mass AGB stars (Ventura et al. 2001) or fast-rotating more massive stars (Decressin et al. 2007) to the proto-stellar clouds of the second generation of stars can produce the observed anticorrelations. Another anticorrelation found within globular clusters is the Mg-Al anticorrelation. However, unlike the Na-O anticorrelation which is found in every globular cluster, the Mg-Al anticorrelation is only found in massive and/or metal-poor globular clusters (Carretta et al. 2009a).

Helium has been suggested to be one of the parameters that determine the different morphologies between globular clusters and their HB evolution with others being metallicity and age (Gratton et al. 2010b; McDonald and Zijlstra 2015b). If stars have been enriched by helium then the nuclear burning luminosity increases during the main

sequence. Consequently the evolution tracks are shifted towards higher luminosities and effective temperatures, and the evolutionary phase lifetimes are significantly shortened. Higher He enrichment (see Chantereau et al. 2015, for examples of multiple $0.8M_\odot$ stars with varying He enrichment between $Y_{ini} = 0.248$ and 0.8 where 0.248 is He values for a normal star) have greater effects on the AGB phase, where the amount of thermal pulses varies and happen in shorter timespans. Above or equal to $Y_{ini} = 0.65$ no thermal pulses occur and models spend a very short time on the AGB (post-early AGB) and evolve directly to the white dwarf stage.

The internal helium variation in globular clusters seems to correlate with both the cluster mass and the colour extension of the HB: massive clusters and globular clusters with very-extended HBs also host stellar populations that are highly helium-enhanced (Milone et al. 2014). It is noted by Milone (2015) that these conclusions are based on a small sample of globular clusters, which includes those objects where high-precision photometry was available to allow the helium measurements from multiple sequences.

1.6.4 The Project

In this thesis, I will be using data obtained from the MIKE spectrograph (§ 1.3.2) with the dates of observations being between 17th July and 26th July with conditions being clear with between roughly 0.5 arcsec and 0.7 arcsec seeing. The setup used was; red and blue CCDs; slow readout; 0.7 inch slit; bin 2x1 (spatial x dispersion) with the exposure being 2 x 1800s. The S/N varied from star to star, and with position in the spectra. For most of the lines investigated, S/N varies between about 50 and 200. Fourteen stars are being investigated, one star from NGC 288, one from NGC 1261, two from NGC 1904 (M79), two from NGC 7078 (also known as M15), three stars from NGC 7089 (M2), four from NGC 7099 (M30) and the final star from NGC 7492. These stars are being investigated to find if they are first or second generation stars and into the affects between AGB and post-AGB stars. Along with this, the project aims to determine the fundamental properties of these stars and the abundances of the elements

currently present within the stars and to check if any foreground stars can possibly be detected and separated from the other stars.

Chapter 2 describes the software and methods used to obtain the iron abundance of the stars and presents the results. Chapter 3 details the results gathered from the other elements in these stars. Chapter 4 describes different methods to obtain more element abundances. Chapter 5 discusses and compares the results gathered to other published work. Chapter 6 summarises the conclusions of this work.

2

Basic Parameters

2.1 Measuring Equivalent Width

The equivalent widths (EWs) of Fe I and II lines were compared to stellar atmospheric models. Fe lines were used as they had a large sample size and are the conventional metallicity indicators. Ti I and II lines could also have been used in principal. By comparing the Fe EWs and the models, the basic parameters for the stars can be obtained, namely: effective temperature (T_{eff}), surface gravity ($\log(g)$), metallicity ([Fe/H]) and the microturbulent velocity (v_{t}).

The programme used to measure the equivalent widths is an updated version of the software used by Johnson et al. (2008). The program uses an input line list and stellar spectrum and allows the user to measure EWs by fitting a Gaussian profile to the absorption lines (Figure 2.1), or multiple Gaussian profiles if the spectral line is blended with other lines (Figure 2.2). A second spectrum can be used as a guide to uncatalogued spectral lines, which can be modified through the user interface to change the temperature, $\log(g)$ and metallicity. The line lists used were collected from previous publications by Christian Johnson (Johnson and Pilachowski 2010b,a; Johnson et al. 2012; Johnson and Pilachowski 2012; Johnson et al. 2013b,a, 2014b,a, 2015) and can be found in Appendix A.
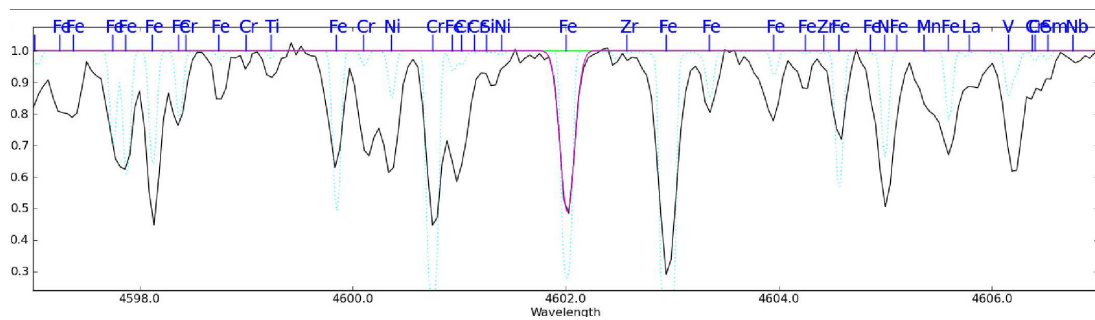
Figure 2.1: The black spectrum is the spectrum of the star being analysed; the light-blue spectrum is the second, guide spectrum; the pink curve is the Gaussian fit for the observed spectrum; the green line represents the continuum level. The elements are shown above to help with identification with respects to blending.
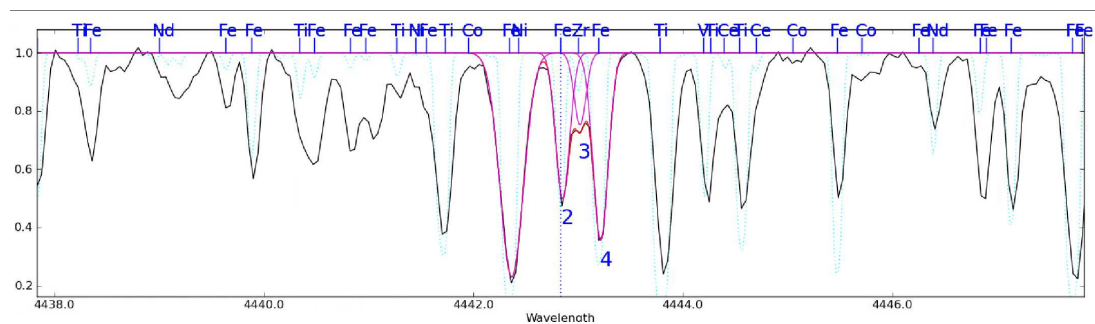
Figure 2.2: Example of deblending. These lines are all very close together and is required to deblend them to get the equivalent width of the iron line accurately. The red line represents the shape of the spectrum with the selected spectral lines.

2.1.1 Wavelength Shifting

Before the EW measurements can proceed there must be some preliminary setup. The spectrum needs to be shifted to its rest velocity to account for the radial velocity of the star and the motion of the telescope compared to the Solar System barycentre, and any errors in the wavelength calibration of the spectrum. However, this does not affect results other than being a visual aid to ensure that the correct lines are being measured.

2.1.2 Continuum

The continuum level in the spectrum must be set in order to achieve more accurate results from measuring the EW. The EW depends greatly on the placement of the

spectral continuum. If the continuum is incorrectly placed, this adds an error to the EW of each spectral line. The error has a greater effect on weaker lines due to having lower EWs. Therefore, a major source of error is in the determination of where the continuum should be set. If the continuum is set too low, then a lot of the weaker lines can be skipped over or have much lower EWs. On the other hand, if it set too high then all lines measured will have an increased EW which greatly affects the weak spectral lines. If the continuum is wrongly set, then this will have an impact on the final parameters, as described in the next section.

2.2 MOOG `abfind`

Once the EWs have been measured for a spectrum, the results can be run through `abfind` which derives the atmospheric parameters for the star by comparing the measured EWs with those of a model atmosphere. The model atmosphere is created using ATLAS9 and involves Kurucz models (Kurucz 1993) and contains four parameters: the effective temperature (T_{eff}), the surface gravity ($\log(g)$), the metallicity ([Fe/H]) and the microturbulent velocity (v_t).

The `abfind` interface features three plots as can be seen in Figure 2.3. The first plot shows $\log(\epsilon)$ versus excitation potential (E.P.). A gradient in this plot is created by differences between the effective temperatures of the star and the model atmosphere. The second plot is $\log(\epsilon)$ against the reduced equivalent width $\log(EW/\lambda)$. A gradient for this plot is created by differences between the microturbulent velocity of the star and model atmosphere. The third plot is $\log(\epsilon)$ against the wavelength.

A model atmosphere with the correct parameters will have blue lines representing the trends in each plot should be flat and match the mean abundance value shown by the yellow line since both of these factors have an impact on the iron abundance. To flatten the trends, the effective temperature and the microturbulent velocity can be modified to affect the first and second plots respectively. The third plot however, cannot be fixed by atmospheric parameters but should not have a significant slope. Sometimes outliers

can appear in the data, these should be removed to make the outcome more reliable.

Outside influences can also affect the plots, the first plot can be affected by non-local thermodynamic equilibrium (non-LTE) processes (e.g. pulsations affect the upper layers of the atmosphere most, where the low E.P. lines absorb the most). The second plot is possibly affected by the continuum placement and can add a curvature to the results.

Once the effective temperature and microturbulent velocity are fixed so that the first two plots are flat, the surface gravity can be determined. Due to Fe I and Fe II just being ionisation states of the same element then both of their abundances must be the same. Therefore, another iteration with $\log(g)$ commences to make these abundances match. This will have a weak effect on the temperature and microturbulent velocity so those should also be corrected throughout the process. Once the abundances are the same and the curves are flat, then the atmospheric parameter values can be taken as final.

2.3   Results

Table 2.1 shows the model atmosphere parameters derived for the stars in the study. This involves the whole spectrum from each star (4000−7000 Å). Table 2.2 shows the results from taking a cut of 5000−7000 Å which produces results closer to the expected values. The results from Table 2.2 will be used for the rest of the project. This is due to the 4000−5000 Å region being heavily blended which impacted the auto-continuum levels making it difficult to get the correct continuum. However, the biggest change is NGC 7089 V6 where the temperature increased by 920K, this is a massive change for only removing a small range of spectrum. NGC 7099 4 has a markedly different radial velocity than the other stars in this cluster. This indicates that it is a foreground star. This is confirmed by its high surface gravity and metallicity. The microturbulent velocity is given to 2 decimal places to fit with other literature.
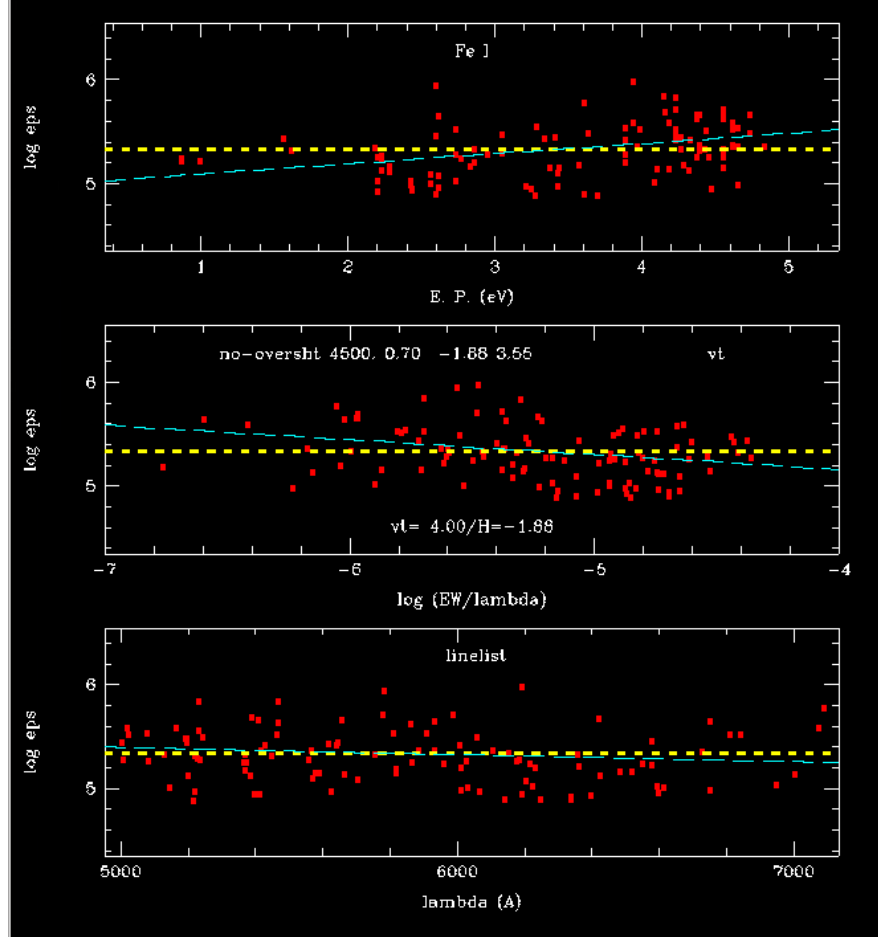
Figure 2.3: The plots produced by MOOG `abfind`. These plots are: the top is $\log(\epsilon)$ against the excitation potential. The middle plot is $\log(\epsilon)$ against the reduced equivalent width. The bottom plot is $\log(\epsilon)$ against the wavelength. The blue curves represent the trend of the data while the yellow line represents the mean value. In this example the temperature would have to be increased while the microturbulent velocity would have to be decreased.

Table 2.1: Results for the basic parameters of the observed stars. This is the whole spectrum for each star. *Neither had useful identifiers.

Cluster NGC	Star	RA (J2000.00)	Dec (J2000.00)	T_{eff} (K)	$\log(g)$ (dex)	[Fe/H] (dex)	v_{t} (km s^{-1})	Fe I (dex)	Fe II (dex)
288	V1	00 52 41.13	–26 33 27.19	3900	0.00	–1.32	2.30	6.20	6.34
1261	V15	03 12 02.50	–55 10 48.10	3750	0.00	–1.31	2.10	5.17	6.23
1904	V2	05 24 16.75	–24 32 34.36	4140	0.00	–1.86	2.45	5.84	5.91
1904	V7	05 24 12.67	–24 31 42.28	5530	0.35	–1.40	2.32	6.13	6.13
7078	K825	21 30 02.25	12 11 21.51	4080	0.00	–2.37	1.98	5.13	5.43
7078	K757	21 30 00.91	12 08 57.13	4180	0.00	–2.26	2.25	5.26	5.27
7089	V1	21 33 28.46	–00 47 55.40	4650	0.50	–1.87	3.67	5.65	5.65
7089	V5	21 33 23.85	–00 49 12.87	4720	0.52	–2.06	3.80	5.44	5.41
7089	V6	21 33 27.52	–00 49 59.58	4680	0.00	–2.19	2.88	5.33	5.67
7099	11294	21 40 21.80	–23 10 09.08	4120	0.00	–2.35	2.20	5.17	5.51
7099	2*	21 40 21.50	–23 09 51.85	3950	0.00	–2.38	2.20	5.19	5.70
7099	AL 155	21 40 03.42	–23 11 44.11	4240	0.00	–2.11	2.15	5.46	5.46
7099	4*	21 40 17.55	–23 15 17.08	5050	2.80	–0.23	1.14	7.29	7.29
7492	V4	23 08 23.18	–15 39 07.09	4080	0.00	–1.76	2.50	5.76	5.77

Table 2.2: Results for the basic parameters of the observed stars. This is the 5000−7000 cut of spectrum for each star.

Cluster NGC	Star	T_{eff} (K)	$\log(g)$ (dex)	[Fe/H] (dex)	v_{t} (km s^{-1})	Fe I (dex)	Fe II (dex)
288	V1	3930	0.10	−1.23	2.03	6.290	6.300
1261	V15	3880	0.00	−1.33	2.13	6.185	6.318
1904	V2	4100	0.00	−1.64	2.52	5.884	6.302
1904	V7	5450	0.70	−1.52	2.82	6.003	5.995
7078	K825	4040	0.00	−2.49	1.68	5.034	5.204
7078	K757	4170	0.12	−2.29	2.12	5.231	5.214
7089	V1	4750	0.75	−1.86	3.85	5.662	5.646
7089	V5	4740	0.70	−1.88	3.55	5.642	5.632
7089	V6	5600	0.70	−1.70	4.10	5.813	5.809
7099	11294	4120	0.00	−2.34	2.05	5.178	5.360
7099	2	4020	0.00	−2.34	2.15	5.165	5.578
7099	AL 155	4170	0.00	−2.09	1.93	5.442	5.573
7099	4	4980	2.70	−0.23	1.04	7.287	7.306
7492	V4	4050	0.00	−1.77	2.41	5.717	5.758

3

Other Elements

The abundance for aluminium (Al), silicon (Si), calcium (Ca), titanium (Ti, I and II), chromium (Cr), nickel (Ni), yttrium (Y) II, zirconium (Zr) II, ruthenium (Ru), cerium (Ce) II, neodymium (Nd) II and europium (Eu) II were also measured along side Fe. This was done in the same manner as that for Fe but using a different line list for the other elements which was also obtained from Christian Johnson's papers (Johnson and Pilachowski 2010b,a; Johnson et al. 2012; Johnson and Pilachowski 2012; Johnson et al. 2013b,a, 2014b,a, 2015). The line list used for this section is shown in Appendix B. The atmospheric parameteres were fixed using the results from Table 2.2.

3.1   Results

[Al/Fe] and [Zr II/Fe] could be determined for 11 out of the 14 stars in this study. [Si/Fe], [Ca/Fe], [Ti/Fe], [Ti II/Fe], [Cr/Fe], [Ni/Fe], [Y II/Fe] and [Nd II/Fe] were determined for all 14 stars. [Ru/Fe] was determined for four stars, [Ce II/Fe] for 12 stars and [Er II/Fe] for only three stars.

MOOG returns abundances as $\log_{10} \epsilon(x)_{star}$, where x represents the elements listed above. The notation [x/Fe] was used to compare abundances and was obtained with the standard relation:

Table 3.1: Solar ϵ element abundances.

Element	Abundance
	A(X)
Na	6.29
O	8.73
Mg	7.54
Al	6.46
Si	7.53
Ca	6.31
Ti	4.93
Cr	5.65
Ni	6.22
Y	2.20
Zr	2.57
Ru	1.78
Ce	1.60
Nd	1.47
Eu	0.95

$$[x/Fe] = [x/H] - [Fe/H]. \tag{3.1}$$

The solar ϵ abundances for these elements are shown in Table 3.1 and were taken from Lodders (2010). The results for the derived abundances are shown in Table 3.2 to Table 3.14 with elements that only have 1 spectral line having an uncertainty of 0.20. The [Ni/Fe] uncertainty for NGC 1904 V7 was higher than expected at 0.30 due to higher noise around the Nickel spectral lines.

Table 3.2: Aluminium results

Cluster	Star	[Al/Fe]	uncertainty in [Al/Fe]	# of lines
288	V1	0.457	0.11	3
1261	V15	0.210	0.03	3
1904	V2	0.473	0.02	3
1904	V7	0.629	0.11	2
7078	K825	0.461	0.14	2
7078	K757	1.355	0.15	3
7089	V5	1.164	0.12	2
7089	V6	0.074	0.20	1
7099	AL 155	0.915	0.05	3
7099	4	0.032	0.03	3
7492	V4	0.595	0.01	2

Table 3.3: Silicon results

Cluster	Star	[Si/Fe]	uncertainty in [Si/Fe]	# of lines
288	V1	0.286	0.17	5
1261	V15	0.406	0.05	8
1904	V2	0.273	0.07	6
1904	V7	0.312	0.17	4
7078	K825	0.441	0.05	6
7078	K757	0.915	0.08	6
7089	V1	0.625	0.15	3
7089	V5	0.479	0.02	3
7089	V6	0.636	0.06	3
7099	11294	0.436	0.02	6
7099	2	0.451	0.09	5
7099	AL 155	0.465	0.07	6
7099	4	–0.038	0.02	8
7492	V4	0.285	0.08	5

Table 3.4: Calcium results

Cluster	Star	[Ca/Fe]	uncertainty in [Ca/Fe]	# of lines
288	V1	0.371	0.09	16
1261	V15	0.292	0.03	17
1904	V2	0.202	0.03	17
1904	V7	1.532	0.13	15
7078	K825	0.411	0.04	17
7078	K757	0.536	0.04	17
7089	V1	0.183	0.06	16
7089	V5	0.341	0.07	16
7089	V6	0.458	0.04	12
7099	11294	0.284	0.03	17
7099	2	0.259	0.03	17
7099	AL 155	0.191	0.03	17
7099	4	0.124	0.05	17
7492	V4	0.289	0.03	17

Table 3.5: Titanium results

Cluster	Star	[Ti/Fe]	uncertainty in [Ti/Fe]	# of lines
288	V1	1.060	0.10	20
1261	V15	1.013	0.05	20
1904	V2	0.159	0.12	20
1904	V7	0.312	0.12	10
7078	K825	–0.011	0.03	19
7078	K757	0.181	0.05	19
7089	V1	0.081	0.09	9
7089	V5	0.325	0.10	8
7089	V6	0.672	0.14	7
7099	11294	0.016	0.03	18
7099	2	–0.036	0.03	18
7099	AL 155	0.032	0.02	18
7099	4	0.128	0.05	20
7492	V4	0.386	0.03	19

Table 3.6: Titanium II results

Cluster	Star	[Ti II/Fe]	uncertainty in [Ti II/Fe]	# of lines
288	V1	0.394	0.15	8
1261	V15	0.461	0.12	8
1904	V2	0.360	0.12	6
1904	V7	–0.041	0.17	7
7078	K825	0.637	0.09	8
7078	K757	0.700	0.10	7
7089	V1	0.008	0.13	6
7089	V5	0.116	0.16	6
7089	V6	0.283	0.06	7
7099	11294	0.566	0.11	8
7099	2	0.583	0.09	8
7099	AL 155	0.350	0.10	8
7099	4	0.282	0.11	8
7492	V4	0.371	0.08	8

Table 3.7: Chromium results

Cluster	Star	[Cr/Fe]	uncertainty in [Cr/Fe]	# of lines
288	V1	0.384	0.12	4
1261	V15	0.215	0.13	4
1904	V2	–0.067	0.34	5
1904	V7	–0.073	0.08	5
7078	K825	–0.376	0.04	4
7078	K757	–0.264	0.10	4
7089	V1	–0.586	0.07	2
7089	V5	–0.441	0.08	3
7089	V6	0.496	0.52	3
7099	11294	–0.462	0.07	4
7099	2	–0.571	0.07	4
7099	AL 155	–0.264	0.16	5
7099	4	–0.020	0.11	4
7492	V4	–0.166	0.09	5

Table 3.8: Nickel results

Cluster	Star	[Ni/Fe]	uncertainty in [Ni/Fe]	# of lines
288	V1	–0.069	0.18	7
1261	V15	0.117	0.06	7
1904	V2	–0.177	0.14	7
1904	V7	0.000	0.30	6
7078	K825	–0.027	0.07	7
7078	K757	0.147	0.10	7
7089	V1	–0.077	0.15	6
7089	V5	–0.210	0.07	6
7089	V6	0.125	0.05	1
7099	11294	–0.107	0.09	7
7099	2	–0.045	0.06	7
7099	AL 155	–0.191	0.04	7
7099	4	0.061	0.05	7
7492	V4	–0.073	0.06	7

Table 3.9: Yttrium II results

Cluster	Star	[Y II/Fe]	uncertainty in [Y II/Fe]	# of lines
288	V1	–0.065	0.04	3
1261	V15	0.526	0.69	4
1904	V2	–0.176	0.12	4
1904	V7	–0.361	0.17	3
7078	K825	–0.049	0.13	4
7078	K757	0.084	0.08	5
7089	V1	0.869	0.29	5
7089	V5	0.038	0.35	3
7089	V6	0.896	0.23	3
7099	11294	–0.051	0.15	3
7099	2	–0.190	0.07	4
7099	AL 155	–0.435	0.07	4
7099	4	–0.210	0.06	5
7492	V4	–0.215	0.04	4

Table 3.10: Zirconium II results

Cluster	Star	[Zr II/Fe]	uncertainty in [Zr II/Fe]	# of lines
288	V1	–0.153	0.20	1
1261	V15	–0.234	0.20	1
1904	V7	–0.161	0.20	1
7078	K825	0.092	0.20	1
7078	K757	0.245	0.20	1
7089	V6	0.658	0.20	1
7099	11294	–0.511	0.20	1
7099	2	–0.063	0.20	1
7099	AL 155	–0.327	0.20	1
7099	4	–0.607	0.20	1
7492	V4	–0.024	0.20	1

Table 3.11: Ruthenium results

Cluster	Star	[Ru/Fe]	uncertainty in [Ru/Fe]	# of lines
288	V1	0.593	0.08	2
1261	V15	0.679	0.05	2
7078	K757	1.377	0.20	1
7089	V1	2.184	0.20	1

Table 3.12: Cerium II results

Cluster	Star	[Ce II/Fe]	uncertainty in [Ce II/Fe]	# of lines
288	V1	0.027	0.13	2
1261	V15	0.084	0.11	2
1904	V2	–0.374	0.20	1
1904	V7	0.113	0.07	2
7078	K825	0.165	0.20	1
7078	K757	0.266	0.20	1
7089	V1	0.626	0.20	1
7089	V6	0.182	0.20	1
7099	11294	–0.034	0.08	2
7099	2	–0.378	0.20	1
7099	4	0.002	0.20	1
7492	V4	0.076	0.05	2

Table 3.13: Neodymium II results

Cluster	Star	[Nd II/Fe]	uncertainty in [Nd II/Fe]	# of lines
288	V1	0.048	0.09	7
1261	V15	0.593	0.13	5
1904	V2	0.127	0.10	4
1904	V7	0.042	0.16	4
7078	K825	0.370	0.05	6
7078	K757	0.625	0.05	6
7089	V1	0.724	0.04	7
7089	V5	0.255	0.11	3
7089	V6	0.851	0.09	5
7099	11294	0.139	0.10	7
7099	2	0.193	0.09	6
7099	AL 155	-0.091	0.06	6
7099	4	0.321	0.13	6
7492	V4	0.146	0.04	6

Table 3.14: Europium II results

Cluster	Star	[Eu II/Fe]	uncertainty in [Eu II/Fe]	# of lines
7078	K825	1.262	0.20	1
7078	K757	1.344	0.20	1
7492	V4	0.381	0.20	1

3.2   Error Analysis

The estimated internal errors were taken to be $T_{\text{eff}} = \pm 100$ K, $\log(g) = \pm 0.20$ dex, [Fe/H] $= \pm 0.20$ dex, $v_{\text{t}} = \pm 0.35$ kms^{-1}. The sensitivity was determined by changing one parameter at a time while keeping the others constant, avoiding extra error due to inter-dependencies among the parameters.

The abundance uncertainty due to atmospheric parameters, σ_{atm}, was calculated using this formula:

$$\sigma_{atm}^2 = \sigma_{T_{\text{eff}}}^2 + \sigma_{\log(g)}^2 + \sigma_{[Fe/H]}^2 + \sigma_{v_{\text{t}}}^2 \tag{3.2}$$

where $\sigma_{T_{\text{eff}}}^2$ is the error due to variations in effective temperature, $\sigma_{\log(g)}^2$ the error due to variations in surface gravity, $\sigma_{[Fe/H]}^2$ the error due to variations in metallicity and $\sigma_{v_{\text{t}}}^2$ the error due to variations in microturbulent velocity.

To get the total error, the error due to model atmosphere parameters, σ_{atm}, and the observational errors, σ_{obs}, which was taken from the mean statistical uncertainties, were added in quadrature as seen in this formula:

$$\sigma_{tot}^2 = \sigma_{atm}^2 + \sigma_{obs}^2 \tag{3.3}$$

The $\log(g)$ values were only based on 5 stars from the 14 available. This is due to being unable to go below 0 when using the ATLAS9 Kurucz models. For [Fe/H] only 11 stars could be used due to being unable to go below [Fe/H] $= -2.5$. The average uncertainties are shown in Table 3.15.

The most influential atmospheric parameter seems to be the effective temperature, having a big impact on both Ti I and Cr but having no affect on Si or Y II. Overall, Si looks to be relatively insensitive to the perturbations of the atmospheric parameters. The surface gravity will affect the ion which is least abundant and is dependent on which ion is most/least present. Singly ionised transition metals are more dependent on electron pressure which is affected more by surface gravity and metallicity. However,

Table 3.15: Abundance sensitivity to model atmosphere parameters.

Abundance	T_{eff}	$\log(g)$	[Fe/H]	v_{t}	σ_{atm}	σ_{tot}
	± 100 K	± 0.20 dex	± 0.20 dex	± 0.35 kms^{-1}	(dex)	(dex)
[Fe/H]$_{\text{I}}$	±0.09	∓0.02	∓0.01	∓0.08	0.12	0.12
[Fe/H]$_{\text{II}}$	∓0.10	±0.08	±0.03	∓0.05	0.14	0.16
[Al/H]	±0.05	∓0.01	∓0.01	∓0.01	0.05	0.09
[Si/H]	±0.00	±0.00	±0.01	∓0.02	0.02	0.08
[Ca/H]	±0.11	∓0.02	∓0.03	∓0.10	0.16	0.16
[Ti/H]$_{\text{I}}$	±0.20	∓0.02	∓0.03	∓0.10	0.23	0.24
[Ti/H]$_{\text{II}}$	∓0.03	±0.07	±0.02	∓0.11	0.14	0.18
[Cr/H]	±0.18	∓0.03	∓0.03	∓0.13	0.23	0.27
[Ni/H]	±0.07	∓0.01	∓0.01	∓0.09	0.11	0.15
[Y/H]$_{\text{II}}$	±0.00	±0.07	±0.03	∓0.09	0.11	0.21
[Nd/H]$_{\text{II}}$	±0.03	±0.07	±0.03	∓0.05	0.09	0.13

in this case, the metallicity has not had a big impact on any particular element. Lastly, the microturbulent velocity has a generally large effect on most elements.

4

MOOG Synth

`Synth` is another part of MOOG and is used when the element abundances derived from transitions involve a small number of lines that are affected by significant blends from prevalent spectral features, such as molecules and/or broadened due to isotopes and/or hyperfine structure. The input parameters are similar to those used with `abfind` but include: abundances changes to specific elements and isotopes. The abundance can be increased or decreased to match the synthetic spectrum acquired from linelists. I start with the same model astmospheres as used in § 2.2. The lines examined can be found in Table 4.1, taken from Johnson et al. (2014b) and were obtained through private communication.

These lines were done through synthesis for different reasons. The 6300.30 Å [O I] line is blended with two other features, a Sc II feature at 6300.69 Å and a Ni I feature at 6300.33 Å. It was also noted that the oxygen abundance is sensitive to the molecular equilibrium calculations set by the carbon and nitrogen abundances as well (Johnson et al. 2014a). Therefore, both the CN and O abundances were iteratively solved, however, with the stars used in this project, the CN abundance did not, or barely, affected the O abundance. The 6160.75 Å Na I line is partially blended with two relatively strong Ca I lines and has variable interstellar components and non-LTE effects. The Mg lines around 6319 Å are strongly affected by a broad Ca I auto-ionisation feature. Auto-ionisation is an excited atom becomes ionised by emitting one of two or

Table 4.1: Linelist that is used in Synth, where E.P. is the excitation potential.

Wavelength	Element	E.P.	$\log(gf)$
6300.304	O I	0.000	-9.75
6154.226	Na I	2.101	-1.56
6160.747	Na I	2.103	-1.21
6318.714	Mg I	5.104	-2.01
6319.237	Mg I	5.104	-2.25
6319.495	Mg I	5.104	-2.73
5889.951	Na I	0.000	0.12
5895.924	Na I	0.000	-0.18

more electrons that together possess more energy that exceeds the atom's ionisation energy. To counteract this, the continuum between 6316 Å and 6320 Å was lowered. The sodium D lines around 5900 Å encountered problems during measurement of the spectra, which will be explained in more detail in section § 4.2.1.

4.1 Measuring Abundances

When running synth, the first thing to do is to line up the observed spectrum with the synthetic spectrum. Unlike abfind, a velocity shift can be set to remove the effects of Doppler motion that will effect the entire spectrum, an example is shown in Figure 4.1. The wavelength can still be shifted, however, it will need to be modified continually. Once the spectral lines are aligned then a smoothing must be applied to the lines. This comes with many options (of which the Gaussian smoothing was used, this 'blurs' the image and removes some detail and noise). The focus on this part is to get the shape correct for most of the lines, other than the one being measured.

Following this, the abundances can be determined. To do this, the elements that are being investigated can have their abundances modified to fit the observed data as seen in Figure 4.2. If a line is blended with other elements, then abundances of both
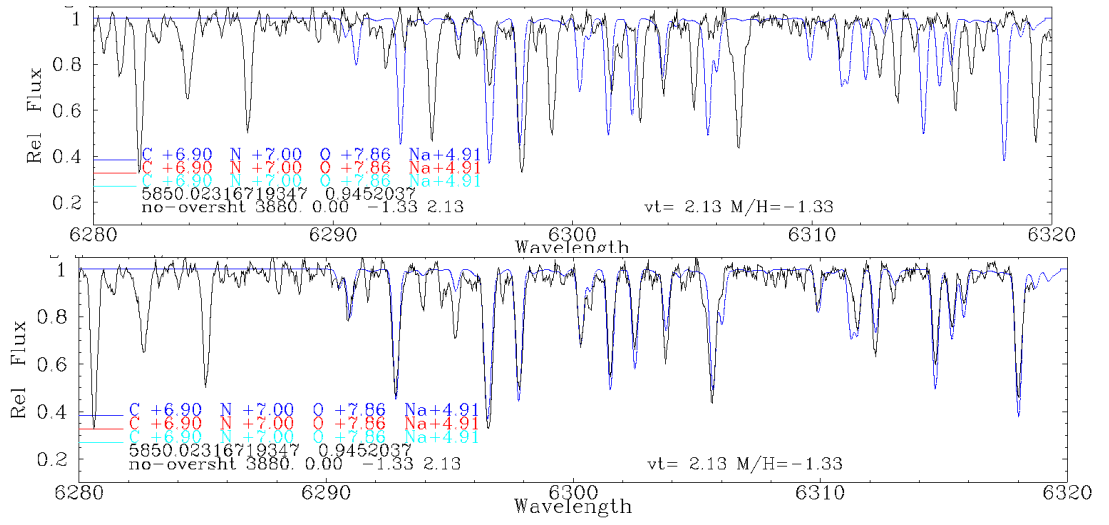
Figure 4.1: Plot taken from `synth`, smoothing has already been applied. The top plot is what is first shown, the blue line is the synthetic spectrum while the black line is the observed spectrum. The bottom plot has been velocity shifted, in this case for NGC 1261 V15, by -63 km/s to align the observed and synthetic spectra.

elements can be modified iteratively to get to the correct abundance. Some of the stars contain spectral lines for specific elements that are not visible above the noise, in this case, an upper limit abundance can be determined.

4.2 Results

4.2.1 Na and O Results

Table 4.2 shows the results for sodium and oxygen along with [O/Na]. The solar ϵ abundances used can be found in Table 3.1. Most of the stars did not have a visible set of Na 6154/6160 Å lines so the results are the upper limit for the abundance. Table 4.2 also shows the results from the sodium D lines. Some of the stars show an offset that can be seen in Figure 4.3 and could be explained by outflow in the envelope that causes the points to be blueshifted. The stars affected by this are NGC 1261 V15, NGC 1904 V2, NGC 288 V1, NGC 7099 2 and NGC 7492 V4. NGC 7089 V1 and NGC 7089 V6 both had a spectral line next to the Na lines so that the resulting abundance is from
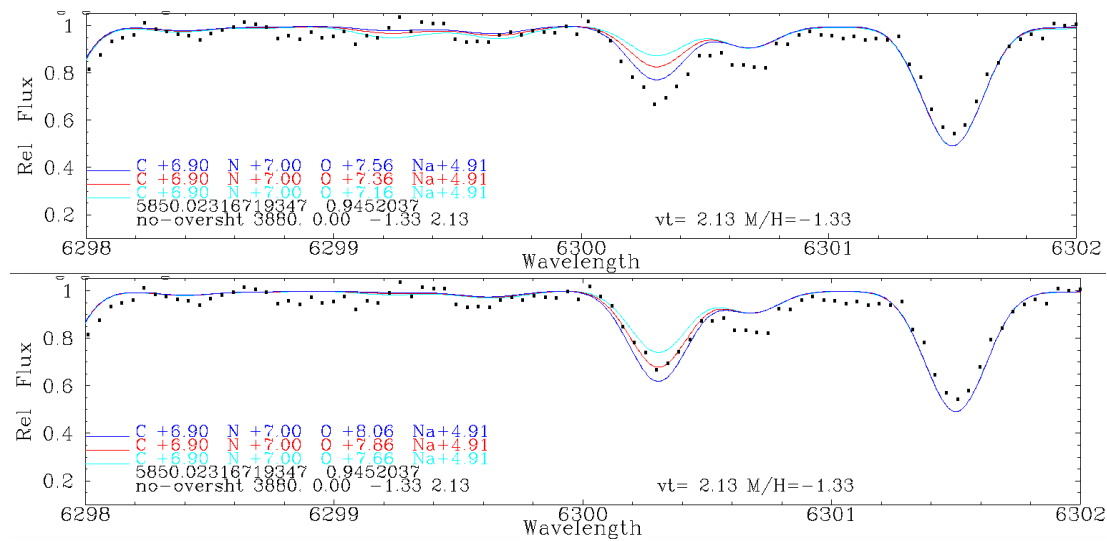
Figure 4.2: Plot showing the changing of abundance in `synth`. The top plot shows the abundance of O to have -0.2 dex from the abundance table (light-blue line), no change, 0 dex (red line) and +0.2 dex (blue line). The O abundance for these changes can be seen at the bottom left of the plot. These values can be repeatedly changed to match up the lines, which is shown in the bottom plot with a change of +0.5 dex which best fits the points. +/- 0.2 dex have been shown for clarity.

fitting the Na line, but is only an estimate. These stars are also expected to have H-alpha emission and substantial mass loss (McDonald and van Loon 2007; McDonald and Zijlstra 2015b).

Table 4.2: The sodium and oxygen results obtained from Synth. The results without errors did not have visible lines and show the estimate of the upper limit abundance. Along with the sodium D results obtained. NGC 1261 V15, NGC 1904 V2, NGC 288 V1, NGC 7099 2 and NGC 7492 V4 are affected by the outflow while NGC 7078 K757 and NGC 7099 AL 155 have the strong emission next to the spectral lines. NGC 7089 V1 and NGC 7089 V6 both have higher errors due to the uncertainty of the effects of the blending spectral line.

Cluster	Star	[Na/H]	Error	[Na/Fe]	[O/H]	Error	[O/Fe]	[Na D/H]	Error
288	V1	−0.78	0.20	0.450	−0.57	0.05	0.660		
1261	V15	−1.38	0.20	−0.045	−0.87	0.05	0.465		
1904	V2	−1.39	0.10	0.246	−1.38	0.10	0.256		
1904	V7	<−1.17		<0.347	<−1.36		<0.157	0.33	0.10
7078	K825	<−2.35		<0.136	−1.94	0.05	0.546	−2.75	0.10
7078	K757	−2.04	0.20	0.249	<−2.33		<−0.041		
7089	V1	−1.41	0.20	0.448	−1.20	0.10	0.658	−0.61	0.30
7089	V5	<−1.43		<0.448	<−1.62		<0.258	−1.43	0.10
7089	V6	<−1.15		<0.557	<−0.94		<0.767	0.55	0.30
7099	11294	<−2.59		<−0.248	−1.78	0.10	0.562	−2.09	0.10
7099	2	<−2.39		<−0.035	−1.78	0.10	0.575		
7099	AL 155	<−1.85		<0.255	−2.04	0.10	0.065		
7099	4	−0.33	0.05	−0.097	−0.17	0.10	0.063	−0.08	0.10
7492	V4	<−1.72		<0.083	−1.41	0.10	0.393		
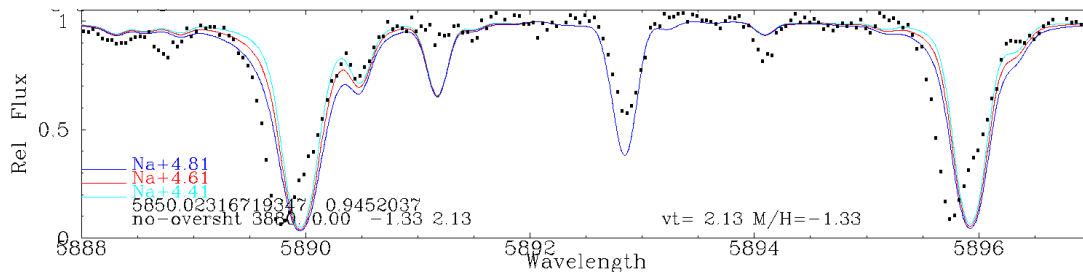
Figure 4.3: Plot obtained from `Synth`, the points on the two Na lines are offset from the synthesised version, which can be better seen from the line on the right at 5896 Å and is thought to be due to outflow.

4.2.2 Mg and Al Results

The results for magnesium and aluminium are shown in Table 4.3. Again for Mg a lot of the stars did not show spectral lines in the region and were taken to be upper limits. For the star NGC 7099 4 the continuum between 6316 and 6320 Å was lowered to reduce the broad Ca I auto-ionisation feature, which was not present in any of the other stars with discernible spectral lines.

4.2.3 Rb Results

Table 4.4 shows the results from `Synth` for rubidium. Measuring the Rb line was a bit troublesome due to it being heavily blended with a Si line next to it. Only NGC 288 V1, NGC 1261 V15 and NGC 7099 4 (foreground star) had any Rb lines, the rest are upper limits.

Table 4.3: The magnesium and aluminium results obtained from Synth. The results without errors did not have visible lines and show the estimate of the upper-limit abundance.

Cluster	Star	[Mg/H]	Error	[Mg/Fe]	[Al/H]	Error	[Al/Fe]
288	V1	–0.87	0.10	0.36	–1.34	0.05	–0.005
1261	V15	–0.97	0.10	0.37	–1.64	0.05	–0.004
1904	V2	–1.28	0.10	0.36	–1.60	0.05	–0.083
1904	V7	<–0.66		<0.86	–1.23	0.10	0.000
7078	K825	<–1.54		<0.95	<–2.50		<–0.014
7078	K757	<–1.43		<0.86	–1.70	0.05	0.589
7089	V1	<–1.20		<0.66	<–1.62		<0.238
7089	V5	<–0.82		<1.06	–1.39	0.1	0.488
7089	V6	<–0.94		<0.77	<–1.41		<0.297
7099	11294	<–1.68		<0.66	<–1.71		<0.632
7099	2	<–1.68		<0.68	<–2.25		<0.105
7099	AL 155	<–1.94		<0.17	–1.61	0.05	0.495
7099	4	–0.17	0.10	0.06	–0.64	0.05	–0.407
7492	V4	<–1.31		<0.49	–1.68	0.05	0.123

Table 4.4: The rubidium results obtained from Synth. The results without errors did not have visible lines and show the estimate of the upper-limit abundance.

Cluster	Star	[Rb/H]	Error	[Rb/Fe]
288	V1	–1.39	0.05	–0.055
1261	V15	–1.59	0.10	0.046
1904	V2	<–1.95		<–0.433
1904	V7	<–0.53		<0.700
7078	K825	<–2.45		<0.036
7078	K757	<–2.25		<0.039
7089	V1	<–2.22		<–0.362
7089	V5	<–1.74		<0.138
7089	V6	<–0.96		<0.747
7099	11294	<–1.86		<0.482
7099	2	<–2.30		<0.055
7099	AL 155	<–1.76		<0.345
7099	4	–0.79	0.05	–0.557
7492	V4	<–2.23		<–0.427

5

Discussion

5.1   Comparing Results to Literature

During this chapter my results will be compared with the stellar parameters obtained in other literature. The results will also be compared with spectral energy distribution (SED) fits by Iain Mcdonald of the temperature and luminosity of the stars. The SED fitting uses the first-order determinations of temperature, luminosity and stellar gravity from blackbody fits to broadband photometry as initial parameters for the synthetic spectra. The data are then compared with a grid of model atmospheres and a linear interpolation is performed in temperature and surface gravity (see McDonald et al. 2009, 2012, for more information). The temperature is fit to within 1K and the effective temperature, luminosity, surface gravity and model photometry are calculated.

Variable stars do change effective temperature during their variability. The SED fittings use photometry taken from multiple epochs, therefore typically approximates the mean temperature. For example, for NGC 1261 V15, a V-band magnitude change of ± 0.11 mag (giving a total range of 0.22 mag) corresponds to a temperature difference of about ± 50 K (=100 K range). This does not cover some of the temperature differences between my results and those found from SED or literature.

The process to achieve the 1K precision (The following is from McDonald et al.

Table 5.1: Temperature results alongside the SED temperatures and luminosities. Also included are the periods, evolutionary stage of the star and the "generation" of star.

Cluster	ID	Period	T_{eff}	SED T_{eff}	SED L	Stage	"Generation"
		Days	K	K	$L_{\odot}$		
288	V1	103	3930	3764	2172	RGB/AGB	Intermediate
1261	V15	80.5	3880	4236	2503	RGB/AGB	Primordial
1904	V2		4100	4750	1780	RGB/AGB	Intermediate
1904	V7		5430			post-AGB	Intermediate
7078	K825	350	4040	4100	1587	RGB/AGB	Int or Prim
7078	K757	250	4170	4200	1458	RGB/AGB	Int or Extreme
7089	V1	15.5647	4750	5295	656	post-AGB	Intermediate
7089	V5	17.557	4740	5200	722	post-AGB	Intermediate
7089	V6	19.299	5600	5667	764	post-AGB	Intermediate
7099	11294		4120	4044	1640	RGB/AGB	Primordial
7099	2		4020	4173	1964	RGB/AGB	Primordial
7099	AL 155		4205	4148	1592	RGB/AGB	Intermediate
7099	4		4980				Foreground Star
7492	V4	21.7	4050	5293	4625	post-AGB	Primordial

2012) first performs on the temperature grid-point immediately cooler than the black-body temperature. Then the χ^2 is calculated for the neighbouring temperature grid-points until a minimum is detected. The new temperature is used as the new start point, a new surface gravity is calculated, and χ^2 is determined for 128K steps between the neighbouring models. A new χ^2 minimum is determined, the temperature step halved, and the process is rerun until the temperature is fit within 1K.

Table 5.1 shows the results for the effective temperature (§2) along with the SED fitting results. Alongside this, the known periods for the stars are shown which is then factored into determining the evolution stage for each star. RGB/AGB stars are expected to have around a T_{eff} of around 4000K (using the results I have obtained) and a luminosity (taken from the SED fitting) of < 2000L$_\odot$ and could either be on the RGB track or on the AGB. It is hard to determine which as their surface properties are very similar. It is thought that NGC 288 V1 and NGC 1261 V15 could be on the RGB tip but not conclusive of being AGB stars. AGB stars will also have a similar temperature but the luminosity is > 2000L$_\odot$. A star with a period < 40-60 days and a temperature closer to 5000K is considered to be a post-AGB star (Kamath et al. 2015). NGC 7492 V4 is expected to be a post-AGB star due to its short period and that my resulting temperature is lower than expected. This comes from unexpected results from MOOG which gave a surface gravity of less than zero, but can only go to zero in MOOG. This gives an inaccurate reading of the temperature due to being unable to match up the Fe I and Fe II abundances. the SED temperature would fit with it being a post-AGB star. NGC 7089 V1, V5 and V6 are classed as post-AGB stars because of their periods and temperatures, however, are not usual post-AGB stars as they have low luminosities.

The equivalent width measurements and abundance measurements are not without their faults and can end up going wrong. The fits are easily affected by the continuum placement which has a big influence on the stellar paraments as well as stray light in fibres in these dense stellar environments. SED fits also rely on having good photometry, which can be challenging at wavelengths where the stars are faint and the surroundings crowded. Another problem is using hydrostatic models for pulsating stars that may not be in LTE. This affects the stellar parameters as the abundances for Fe I and Fe II are "forced" together by altering the parameters which can be impacted by one or the other abundance being lower or higher than expected. Lapenna et al. (2014) found that during their investigation of 47 Tucanae AGB stars suffered from departures from the LTE conditions, which mainly affects the less abundant species which was Fe I in their case. This caused the Fe I abundance values to be less than the Fe II abundances. The

effects of non-LTE are predicted to increase for decreasing metallicity and for decreasing atmospheric densities (i.e., lower surface gravities at a given T_{eff}), however not all stars are affected by this. Johnson et al. (2015) also had four AGB stars in common with Lapenna et al. (2014) and found that the most discrepant abundances were [Fe I/H] while the [Fe II/H] abundances were similar. They also encountered seven of their AGB stars to fail in converging to a stable spectroscopic solution. I will now address each star individually and compare my results with values found in literature and SED fitting.

5.1.1 NGC 288

V1

Variability in V15 was discovered by Oosterhoff (1943) with a period of 103 days with an amplitude of δM : 0.22 mag (Arellano Ferro et al. 2013). The stellar parameters that have been obtained are;

- My results : T_{eff} = 3930K, log(g) = 0.1 dex, [Fe/H] = –1.23 dex and v_{t} = 2.03 km s^{-1}.

- From Smith et al. (1999) : T_{eff} = 3750K, log(g) = 0.5 dex, [Fe/H] = –1.28 dex.

- From Shetrone and Keane (2000) : T_{eff} = 3780K, log(g) = 0.1 dex, [Fe/H] = –1.31 dex and v_{t} = 1.6 km s^{-1}. Also found significant Na D core shifts.

- SED fit by Iain McDonald : T_{eff} = 3764K.

Comparing the results, mine come out with a higher temperature and microturbulent velocity but with reasonable values for surface gravity and metallicity. The higher temperature and microturbulent velocity could be an effect from either one of them being higher than expected as they both impact on each other. When comparing my results alongside the SED temperature it shows that my temperature is higher than it

should be by greater than the expected errors (± 70-100K). It is not expected that the effective temperature would change much during the variability.

I think this could have been affected by a misplaced continuum setting that caused v_t to be higher, which impacts the temperature. This can also be seen when comparing my results with those from Shetrone and Keane (2000) as they found a v_t of 1.6 km s^{-1}. Smith et al. (1999) used model atmospheres interpolated using the MARCS models produced by Gustafsson et al. (1975). They also used both photometry and spectroscopy to obtain T_{eff}, using a spectroscopic analysis of Fe I and Fe II lines. Shetrone and Keane (2000) calculated T_{eff} and the surface gravity through colour values. Both assumed a mass of roughly 0.8M$_\odot$.

5.1.2 NGC 1261

V15

Variability in V15 was discovered by Bartolini et al. (1972). It has a period of 80.5 days and an amplitude of 1.1 mag (Wehlau and Demers 1977). There were no stellar parameters in the literature to compare my results to, therefore I can only compare my results with the SED fitting. The SED fit T_{eff} = 4236K. My T_{eff} was a lot lower than this value, at only 3880K, however the surface gravity I obtained is expected to be <0 dex and therefore a lot lower than expected. This would greatly affect the effective temperature and metallicity. The Fe I and Fe II abundance values are -1.33 and -1.20 respectively with a cluster metallicity of [Fe/H] = -1.27.

5.1.3 NGC 1904 - M79

V2

Bailey (1902) discovered V2, however, not much is known about it. It is a semi-regular variable with an amplitude of 0.6 mag (Rosino 1952) with no period estimate. Even in the major paper by Kains et al. (2012) on the variable stars in NGC 1904, V2 and

V8 were saturated in their reference images. Again, I can only compare my effective temperature of 4100K to that from the SED fitting which was 4750K. Similar to that of V15 from NGC 1261, the surface gravity value is even more negative, with Fe I and II abundances being -1.64 to -1.22 and has a cluster metallicity of [Fe/H] = -1.6. I do not think that a negative gravity is feasible, with the stellar parameters being affected, possibly by non-LTE effects.

V7

The variable star was first identified by Tsoo Yu Hua, who reported it to Sawyer Hogg in a letter in 1965 (Clement 2010). In her 3rd catalogue, Sawyer Hogg (1973) assigned V7 to the star. The amplitude for V7 is 0.7 mag and shows long-term variability with its location on a CM diagram indicating that it might be a long period type II Cepheid (Kains et al. 2012). The T_{eff} I obtained was 5430K with [Fe/H] = -1.52 dex with a surface gravity of 0.7 dex and microturbulent velocity of 2.82 km s^{-1}. There is nothing to compare my results to except the cluster metallicity (which is -1.6) as there is insufficient photometric data for an SED fit. However, the results that I get are in keeping with those expected for a post-AGB star.

5.1.4   NGC 7078 - M15

K825

The variability was proposed by Mosley and White (1975). Welty (1985) later retained K825 as a candidate variable. Variability was later confirmed by McDonald et al. (2010) with a period of 350 days and an amplitude of 0.15 mag. The results for the stellar parameters are;

- My results : T_{eff} = 4040K, log(g) = 0.00 dex, [Fe/H] = -2.49 dex and v_{t} = 1.68 km s^{-1}.

- From Sneden et al. (2000) : T_{eff} = 4275K, log(g) = 0.65 dex, [Fe/H] = -2.28 dex.

- From McDonald et al. (2010) : $T_{\text{eff}} = 4411\text{K} \pm 155\text{K}$.

- From Worley et al. (2013) : $T_{\text{eff}} = 4325\text{K}$, $\log(g) = 0.52$ dex, [Fe/H] = -2.32 dex and $v_{\text{t}} = 2.40$ km s^{-1}.

- SED fitting by Iain McDonald : $T_{\text{eff}} = 4100\text{K}$.

My temperature, along with surface gravity are a lot lower than the rest of the stellar values from the literature along with the microturbulent velocity. The temperature matches closely with the SED fitting. For my results to be so far from those seen in other literature I can only assume that the continuum level was incorrect, however there could have been other factors for there to be such a big impact on the results. This could be from measuring the ionisation balance of Fe I and Fe II which can be affected by non-LTE effects.

In the work by Sneden et al. (2000) they converted B–V into T_{eff} and mass into $\log(g)$ along with keeping v_{t} constant at 2.0 km s^{-1}. Worley et al. (2013) used a two-step process involving a relation between T_{eff} and the V (or K_{s}) magnitudes that was developed using $V - K$ photometry and the Alonso et al. (1999) calibration, which was then used for each star. The $\log(g)$ was calculated using this T_{eff}, the apparent magnitude, the distance modulus and bolometric corrections from Alonso et al. (1999). In contrast mine were done by measuring the ionisation balance between Fe I and Fe II, with Fe I possibly being affected by non-LTE effects.

K757

The variability for K757 was proposed Mosley and White (1975) and later confirmed by McDonald et al. (2010) along with a period of 250 days and an amplitude of 0.15 mag. The stellar parameter results that I obtained and found in literature are as follows;

- My results : $T_{\text{eff}} = 4170\text{K}$, $\log(g) = 0.12$ dex, [Fe/H] = -2.29 dex and $v_{\text{t}} = 2.12$ km s^{-1}.

- From Sneden et al. (2000) : $T_{\text{eff}} = 4275\text{K}$, $\log(g) = 0.65$ dex, [Fe/H] = -2.37 dex.

- From McDonald et al. (2010) : T_{eff} = 4489K ± 201K.

- From Worley et al. (2013) : T_{eff} = 4338K, log(g) = 0.58 dex, [Fe/H] = -2.27 dex and v_{t} = 2.90 km s^{-1}.

- SED fitting by Iain McDonald : T_{eff} = 4200K.

Even though the metallicity I got is close to other literature, my surface gravity is again a lot lower than it should be. This looks to lower both temperature and the microturbulent velocity. However, when comparing the temperature to the SED fit then my result matches quite closely with that temperature. However, K757 has similar problems as K825.

5.1.5   NGC 7089 - M2

The three variable stars examined in NGC 7089 were confirmed by Bailey (1902) with all three being Cepheid Variable stars. The periods and amplitudes are from Lee and Carney (1999).

V1

The period and amplitude for V1 are 15.5647 days and 1.1 mag respectively. No other stellar parameters are available in the literature, so my effective temperature and metallicity can only be compared with the SED fitting. My results being T_{eff} = 4750K, [Fe/H] = -1.86 dex, log(g) = 0.75 dex and v_{t} = 3.85 km s^{-1} compared the temperature from the SED fit of 5295K and the cluster metallicity of -1.65. I have a lower temperature and high metallicity. However, the quality of photometry for the stars was poor and could have affected the effective temperature from the SED fit which could have brought down the temperature.

V5

The only information that could be obtained for this star was the period and the amplitude. The period for V5 is 17.557 days with the amplitude being 0.85 mag (Lee and Carney 1999). No other literature has worked out the stellar parameters for V5. My results for V5 are; T_{eff} = 4740K, log(g) = 0.70 dex, [Fe/H] = -1.88 dex and v_{t} = 3.55 km s^{-1} and can be compared with 5200K from the SED fitting. My temperature is lower than that found from the SED fit but had poor data quality which could affect the temperature attained.

V6

The period for V6 is 19.299 days with an amplitude of 1.0 mag (Lee and Carney 1999). Same as V5 there is no other stellar parameter values in the literature. My results for the stellar parameters for V6 came out to be; T_{eff} = 5600K, log(g) = 0.70 dex, [Fe/H] = -1.70 dex and v_{t} = 4.10 km s^{-1}. This is a lot closer to the values from the SED which came out to be 5667K and the metallicity is closer to that of the cluster value.

5.1.6 NGC 7099 - M30

These stars were selected for observation because they are near the RGB tip, unlike the other stars which were selected on the basis of their variability.

NGC 7099 01

Carretta et al. (2009b) obtained stellar parameters for NGC 7099 01 (my designation) under their identifier of 11294. Their results were; T_{eff} = 4258K, log(g) = 0.41 dex, [Fe/H] = -2.37 dex and v_{t} = 2.14 km s^{-1}. My results for this star are T_{eff} = 4120K, log(g) = 0.00 dex, [Fe/H] = -2.34 dex and v_{t} = 2.05 km s^{-1} along with SED fit giving T_{eff} = 4044K. My metallicity and microturbulent velocity match up fairly well with the values from Carretta et al. (2009b). However, my surface gravity is too low and my

effective temperature more closely matches that of the SED fit. This could be caused by non-LTE effects on the Fe I abundance.

NGC 7099 02

No literature can be found on this star. My results for this star are; T_{eff} = 4020K, log(g) = 0.00 dex, [Fe/H] = -2.34 dex and v_{t} = 2.15 km s^{-1} with the effective temperature from the SED fit being 4173K. I believe the surface gravity is too low again, which would lower the temperature.

NGC 7099 AL 155

Through the study of photometric data taken between November 1984 and September 1987, Geisler (1988) calculated the temperature of AL 155 to be 4140K. My results on this star are T_{eff} = 4205K, log(g) = 0.00 dex, [Fe/H] = -2.10 dex and v_{t} = 1.99 km s^{-1} which matches quite closely to the temperature found by Geisler. It also matches quite well with the effective temperature of 4148K calculated in the SED fitting by Iain McDonald. However, the surface gravity again is at 0 from balancing the Fe I and II abundances.

NGC 7099 04

There have been a few papers but they only contain colour-magnitude diagrams and no specific information on this star. My stellar parameters for this star are; T_{eff} = 4980K, log(g) = 2.70 dex, [Fe/H] = -0.23 dex and v_{t} = 1.04 km s^{-1}. With the radial velocity being markedly different from the other stars in this cluster, indicating that this is a foreground star. This is then confirmed by its high surface gravity and metallicity. This proves that the star is a foreground star and while it is not of much interest in this project, it is still good to be able to identify the star as as such in NGC 7099. The photometric data were of insufficient quality to obtain an accurate SED fit.

5.1.7   NGC 7492

V4

The variability of V4 was first confirmed by Barnes (1968). In his ID charts, V4 is Star G which is located in Ring 3, Sector 4. The x,y coordinates were later derived by Sawyer Hogg (1973) in her third catalogue. V4 is classified as a long-period variable. The period of 21.7 days and an amplitude of 0.18 mag were obtained by Figuera Jaimes et al. (2013). No stellar parameters have been obtained for V4 from literature, my results are; T_{eff} = 4050K, log(g) = 0.00, [Fe/H] = -1.77, v_{t} = 2.41. When compared with the SED fitting, there is a huge difference between the temperatures, with the temperature from the SED fit being 5293K. The SED temperature is more likely to be accurate than my value due to the short period and high luminosity (Table 5.1) making this a post-AGB star which usually requires a temperature of roughly 5000K.

5.2   Multiple Populations

5.2.1   Other Elements

Table 5.2 shows the average abundances for each cluster for some of the elements from §3. This is compared with two clusters from Roediger et al. (2014), which is a compilation of abundances from the literature on globular clusters. Only two of my clusters were included in the compilation. The metallicities from Harris (1996, 2010 edition) are also shown. The two bold abundances do not agree within errors. It is thought that the log(g) values are the reason. This leads to having the wrong model parameters for the star, which means that the all the abundances will be incorrect. The ions least populated will be the most affected. The σ value for NGC 1904 is higher than other GCs as V2 had a [Ca/Fe] value of 0.202 while V7 had a value of 1.532.

Table 5.2: Comparison of some other element abundances and metallicity. The two bold values are higher/lower than expected.

NGC ID	[Fe/H] dex	[Ca/Fe] dex	σ	[Si/Fe] dex	σ	[Cr/Fe] dex	σ	[Ti/Fe] dex	σ
288	−1.23±0.10	0.37±0.13	0.09	0.29±0.17	0.17	0.38±0.08	0.12	1.06±0.12	0.10
1261	−1.33±0.10	0.29±0.09	0.03	0.41±0.17	0.05	0.22±0.12	0.13	1.01±0.10	0.05
1904	−1.58±0.06	**0.87±0.03**	0.94	0.29±0.06	0.03	−0.07±0.24	0.00	0.24±0.09	0.11
7078	−2.39±0.10	0.24±0.04	0.09	0.68±0.06	0.34	−0.32±0.07	0.08	**0.09±0.04**	0.14
7089	−1.81±0.11	0.33±0.06	0.14	0.58±0.08	0.09	−0.51±0.07	0.10	0.36±0.11	0.30
7099	−2.26±0.16	0.24±0.03	0.05	0.45±0.06	0.01	−0.43±0.10	0.16	0.00±0.03	0.04
7492	−1.77±0.10	0.29±0.03	0.03	0.29±0.08	0.08	−0.17±0.09	0.09	0.39±0.03	0.03
Results from Roediger et al. (2014).									
1904	−1.58±0.12	0.22±0.04		0.28±0.03		−0.28±0.14		0.22±0.10	
7078	−2.39±0.14	0.31±0.14		0.48±0.20		−0.23±0.08		0.48±0.20	
7089	−1.64±0.08								
Metallicities from Harris (1996, 2010 edition).									
288	−1.32								
1261	−1.27								
1904	−1.60								
7078	−2.37								
7089	−1.65								
7099	−2.27								
7492	−1.78								

5.2.2 Na/O

Figure 5.1 plots the [Na/Fe] and [O/Fe] abundances of my data. Data from Johnson and Pilachowski (2012) on M13 is also shown to help identify primordial (first), and intermediate and extreme (later) generations of stars. The precise generation cannot be obtained easily for NGC 7078 K825 and K757 along with NGC 7492 V4 due to only having upper limits and therefore not knowing the exact location of the star. NGC 7099 4 is not classified under these circumstances as it is a foreground star.

The Na/O anticorrelation is a good tracer of enrichment of second-generation stars, including He enrichment (Johnson and Pilachowski 2012). The He enrichment is thought to come from the primordial stars which pollute the cluster with newly created material including newly synthesized He. This causes second-generation stars to become He-rich which burn faster. The current He-rich AGB stars therefore have a lower mass than He-poor AGB stars. This leads to the AGB tip that should occur earlier and at a lower luminosity.

Figure 5.1 shows the measured sodium and oxygen abundances (see Table 4.2), where the grey arrows indicate the upper limits. The first plot uses the results obtained from the 6154/6160 Å Na lines, which line up well with the sequence found by Johnson and Pilachowski (2012) in M13. Most of the stars are either primordial or intermediate. The exception is NGC 7078 K757 which could be an extreme star due to having a high sodium abundance and negative oxygen abundance. The second plot in Figure 5.1 shows the Na D lines. Only a few of the stars lie within "normal" ranges while the rest have extreme sodium values. The Na D results are unexpectedly high and do not follow the Na/O sequence of M13. The results from the Na D lines do not seem to be a useful indicator. This is likely because they are low excitation lines that lie high up in the pulsating atmosphere where they are subject to effects not probed by the hydrostatic model atmospheres.
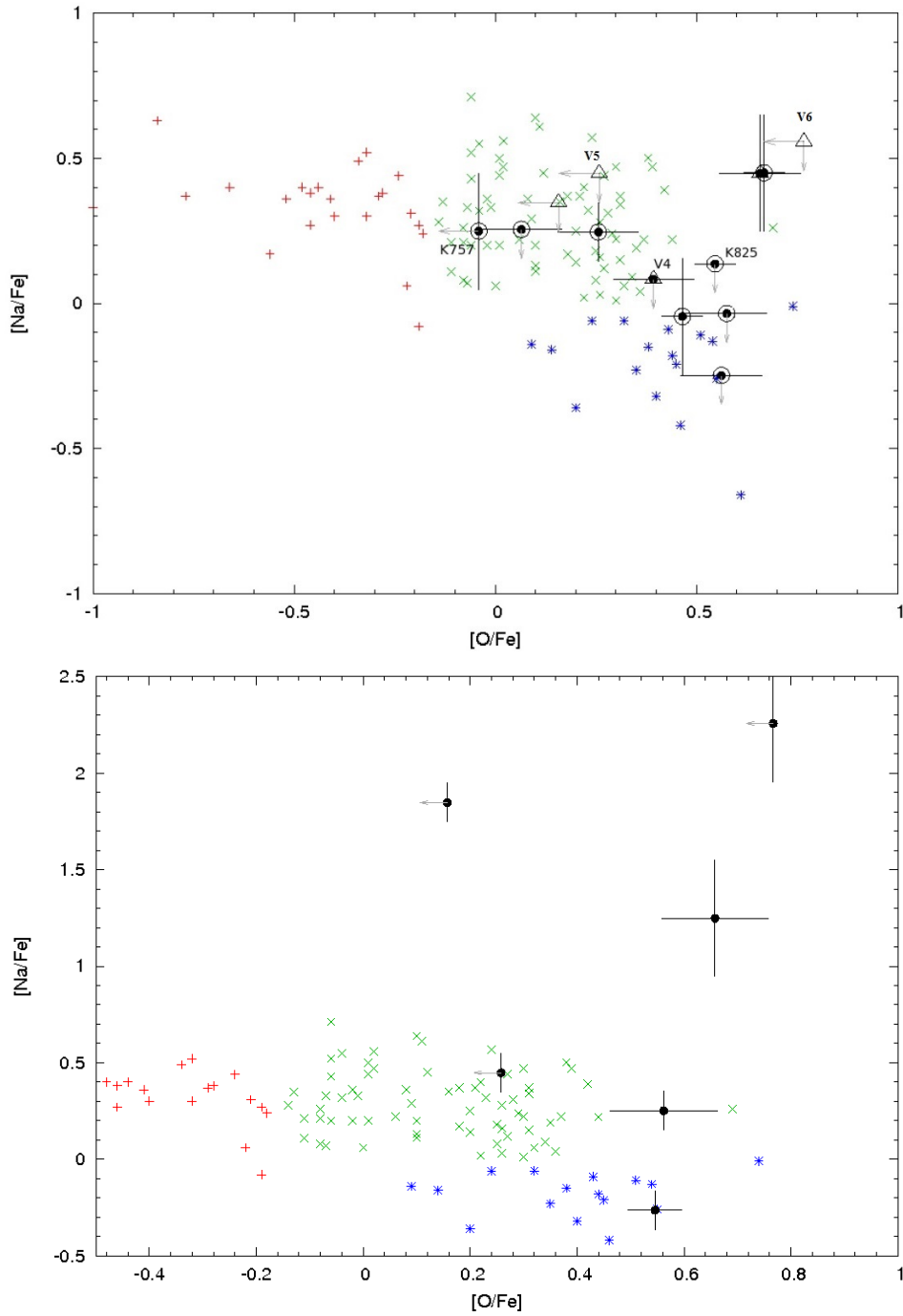
Figure 5.1: Na/O plot using the 6154/6160 Å Na lines, the grey arrows indicate the upper limits that were obtained. The red, green and blue points are from Johnson and Pilachowski (2012) on M13. Extreme, intermediate and primordial stars are shown by red, green and blue respectively. The stage of the stars are denoted by a circle for RGB/AGB stars and a triangle for post-AGB stars. The second plot uses the Na D lines.

5.2.3 Mg/Al

Figure 5.2 plots the [Mg/Fe] and [Al/Fe] abundances of my data. Data from Carretta et al. (2012) on NGC 6752 for comparison. As seen in Figure 5.1, RGB/AGB stars are represented by a circle and post-AGB stars are represented by a triangle. The colours of each correspond to the "generation" of the star. Again NGC 7099 4 has been left out as it is a foreground star.

The Mg and Al results add confirmation of the generations found for each star. When comparing Mg/Al with the Na/O results, NGC 7492 V4 is identified as being a primordial star. The Mg/Al anticorrelation is not found in every globular cluster (Shetrone 1996; Denissenkov and Herwig 2003). This means that the points below around [Al/Fe] $\approx$ 0.4 dex are going to be a mixture of primordial and intermediate stars while points above this will only be intermediate or extreme, which Figure 5.2 shows. K757 and K825 came out with unexpected and interesting Mg/Al values that, despite being similar stars (see McDonald et al. 2010), are apparently different generations.
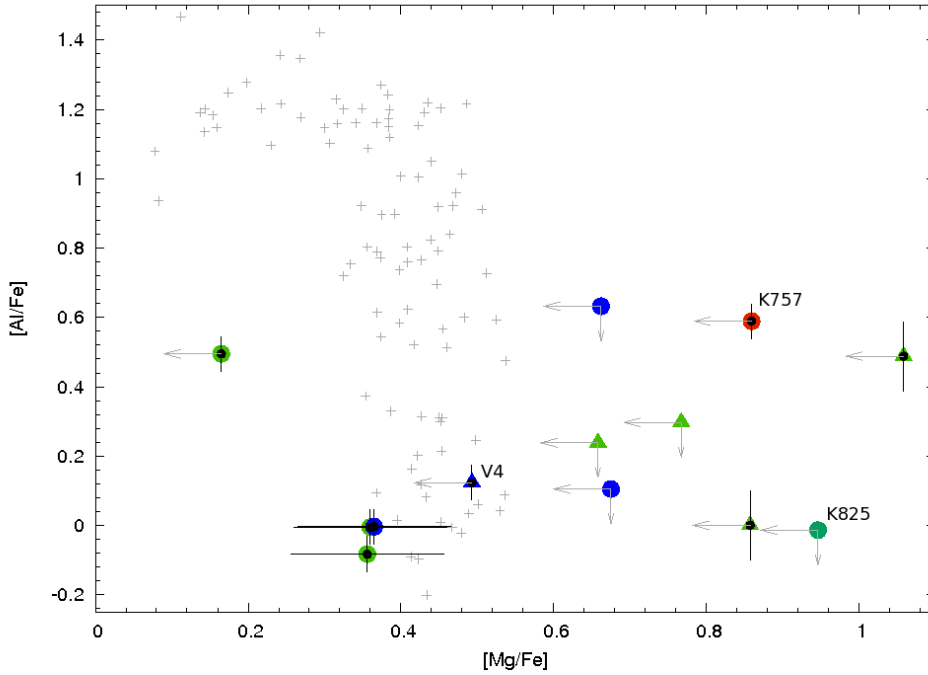
Figure 5.2: Mg/Al plot, the grey arrows indicate the upper limits that were obtained. The grey points are from Carretta et al. (2012) on NGC 6752. The stage of the stars are denoted by a circle for RGB/AGB stars and a triangle for post-AGB stars. They are coloured according to their "generation" (Figure 5.1) with blue being primordial, green being intermediate and red being extreme. The points with colours between these sets as it is uncertain about their generation as there are only have upper limits to the abundances.

5.2.4 Hertzsprung-Russell diagrams

Figure 5.3 is a Hertzsprung–Russell diagram of the SED fits by Iain McDonald (priv. comm.; see Section 5.1) including data from 47 Tucanae (McDonald et al. 2011) and M5 (McDonald et al. in prep.). The first plot has the points showing the generation of each star, with the same colour scheme as Figure 5.1, with the dual symbols denoting stars which could be assigned to more than one generation having both colours. The second plot has the points coloured depending on their cluster metallicity. The giant branches show little spread in Figure 5.3, despite spanning a range in metallicity.

The more interesting points in Figure 5.3 are the stars labelled NGC 7492 V4, NGC 7089 V5 and NGC 7089 V6. These three stars are all considered post-AGB stars
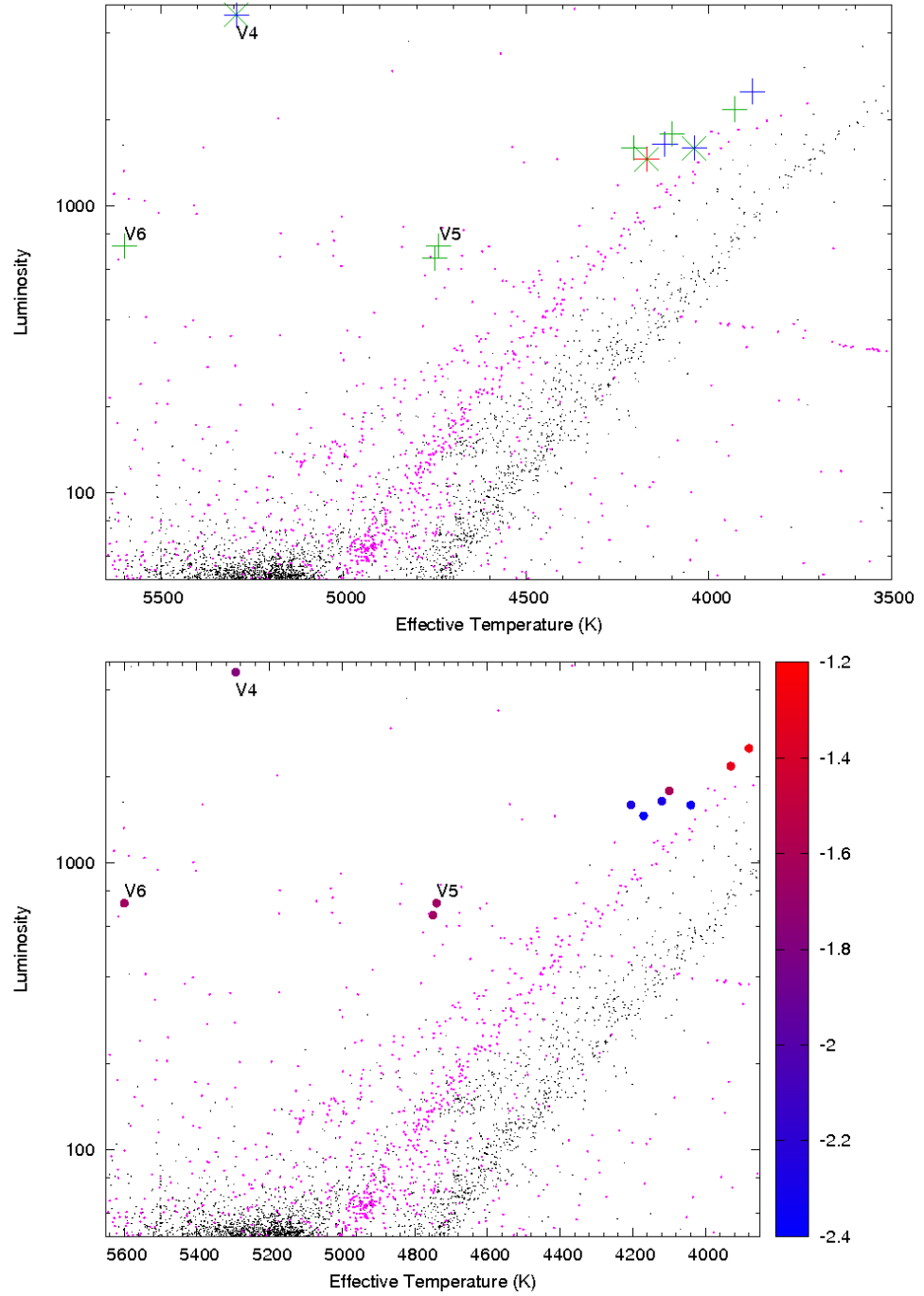
Figure 5.3: Hertzsprung–Russell diagrams. The black and pink dots represent data from NGC 108, or 47 Tucanae (McDonald et al. 2011) and M5 (McDonald et al. in prep.) respectively. The first plot is the same colour scheme as Figure 5.1, the stars that are possibly one or the other generation have both colours together, e.g. V4 could be intermediate or primordial. The second plot has the points coloured depending on their cluster metallicity with the gradient on the side.

within clusters of similar metallicity. In the top plot of Figure 5.1, V5 and V6 are both more extreme so that they are second-generation stars. Therefore, they ought to be He-rich and would have evolved quicker. By the time they get to the AGB they would have a lower mass than stars without He-enrichment. Therefore, it is expected that the AGB-tip turnoff will occur at a lower luminosity as seen in Figure 5.3. This can be compared with V4 which is considered a "normal" primordial star without He-enrichment and therefore a greater luminosity.

5.2.5 Rubidium

Only NGC 288 V1 and NGC 1261 V15 were found to have a measurable rubidium line. An upper limit for Rb was obtained for the remaining stars. D'Orazi et al. (2013) measured Rb in three globular clusters and found typical values between $-0.15 <$ [Rb/Fe] < 0.05. The results from V1 and V15 plus the foreground star compare well with these values. Of the other stars, NGC 1904 V2, NGC 7089 V1 and NGC 7492 V4 stand out with being very deficient in Rb. However, the cause for this is unknown.

6

Conclusions

In this project, the stellar parameters were determined for 14 stars in the direction of seven globular clusters. The abundances were also determined for Al, Si, Ca, Ti I and II, Cr, Ni, Y II, Zr II, Ru, Ce II, Nd II and Eu II. From this, NGC 7099 4 has been classified as a foreground star and the evolution stage was found for the other stars. However, there were problems with obtaining the correct surface gravity values which caused the other stellar parameters to differ from the expected values in some cases.

The generation of each star in the GCs was found using the results for Na and O, by comparison to the data and classifcations from Johnson and Pilachowski (2012) of stars in M13 . The abundances of Mg and Al back up the generations assigned from the Na/O abundances. Five stars were found to be post-AGB stars, one of which only has an associating temperature while the other four have periods and temperatures that relate to being post-AGB. However, the post-AGB stars in NGC 7089 have low luminosities that is not usual in post-AGB stars. NGC 7492 V4 is a normal primordial Post-AGB star with high luminosity. When compared with NGC 7089 V5 and V6, which are potentially extreme second-generation stars, I conjecture that V5 and V6 are He-enhanced due to having turned off the AGB with much lower luminosities.

Only NGC 288 V1 and NGC 1261 V15 had measurable rubidium lines. These were in line with the results found by D'Orazi et al. (2013) from three globular clusters. NGC 1904 V2, NGC 7089 V1 and NGC 7492 V4 were all found to be deficient in Rb

without any known cause.

Appendix A

Fe I and II line list

Table A.1: Linelist for the Fe I and II lines where I.S. is ionization state and E.P. is excitation potential.

Wavelength	Element and I.S.	E.P.	log(gf)
4442.83	26.0	2.176	–2.812
4443.19	26.0	2.858	–1.243
4445.47	26.0	0.087	–5.451
4447.13	26.0	2.198	–2.754
4454.38	26.0	2.831	–1.409
4456.33	26.0	3.047	–2.311
4458.08	26.0	3.884	–1.321
4471.68	26.0	0.110	–5.925
4478.02	26.0	2.198	–3.900
4481.61	26.0	3.686	–1.720
4484.22	26.0	3.602	–0.924
4485.68	26.0	3.686	–1.210
4485.97	26.0	3.654	–2.520

4487.74	26.0	3.237	–3.110
4489.74	26.0	0.121	–3.956
4502.59	26.0	3.573	–2.360
4510.82	26.0	3.602	–2.890
4514.18	26.0	3.047	–2.250
4523.40	26.0	3.654	–2.000
4525.86	26.0	2.882	–3.280
4527.78	26.0	3.251	–2.690
4531.15	26.0	1.485	–2.175
4543.22	26.0	3.640	–3.332
4547.85	26.0	3.546	–1.132
4551.65	26.0	3.943	–2.040
4554.45	26.0	2.865	–3.030
4556.92	26.0	3.251	–2.750
4566.51	26.0	3.301	–2.326
4574.22	26.0	3.211	–2.530
4575.78	26.0	3.301	–3.272
4587.13	26.0	3.573	–1.847
4593.52	26.0	3.943	–2.060
4598.74	26.0	3.654	–2.620
4602.00	26.0	1.608	–3.154
4614.20	26.0	3.301	–2.960
4626.76	26.0	2.990	–3.740
4630.12	26.0	2.279	–2.547
4635.85	26.0	2.845	–2.458
4636.67	26.0	3.047	–3.750
4637.50	26.0	3.283	–1.310
4641.22	26.0	2.832	–3.214
4643.19	26.0	1.485	–5.090

4643.46	26.0	3.654	−1.277
4657.58	26.0	2.845	−3.110
4658.29	26.0	3.267	−2.980
4661.32	26.0	2.831	−4.130
4661.53	26.0	4.558	−1.250
4661.97	26.0	2.990	−2.592
4672.83	26.0	1.608	−4.260
4678.85	26.0	3.602	−0.723
4683.56	26.0	2.831	−2.599
4685.02	26.0	2.845	−3.410
4690.14	26.0	3.686	−1.685
4690.37	26.0	1.011	−5.260
4700.16	26.0	4.320	−1.721
4704.95	26.0	3.686	−1.500
4705.46	26.0	3.546	−2.290
4706.30	26.0	3.642	−2.980
4707.27	26.0	3.241	−0.820
4707.49	26.0	2.845	−2.364
4733.59	26.0	1.485	−2.998
4735.84	26.0	4.076	−1.235
4736.77	26.0	3.211	−0.542
4741.53	26.0	2.831	−2.025
4765.48	26.0	1.608	−3.690
4771.70	26.0	2.198	−3.434
4776.07	26.0	3.301	−2.750
4782.79	26.0	3.237	−3.790
4786.81	26.0	3.017	−1.486
4787.49	26.0	3.018	−4.192
4787.83	26.0	2.998	−2.750

4788.76	26.0	3.237	−1.933
4789.65	26.0	3.546	−0.968
4793.96	26.0	3.047	−3.570
4794.35	26.0	2.424	−4.040
4799.41	26.0	3.640	−2.210
4800.13	26.0	3.038	−3.220
4802.52	26.0	4.607	−1.790
4808.15	26.0	3.251	−2.740
4838.08	26.0	3.251	−3.210
4839.54	26.0	3.267	−1.962
4874.35	26.0	3.071	−3.010
4875.88	26.0	3.332	−2.010
4877.60	26.0	2.998	−3.080
4882.14	26.0	3.417	−1.580
4885.43	26.0	3.882	−1.181
4886.33	26.0	4.154	−0.863
4892.86	26.0	4.217	−1.380
4896.44	26.0	3.883	−2.060
4907.73	26.0	3.430	−1.880
4908.03	26.0	4.218	−1.697
4909.38	26.0	3.929	−1.341
4910.02	26.0	3.397	−1.268
4910.32	26.0	4.191	−0.779
4910.56	26.0	4.218	−0.823
4911.53	26.0	4.256	−1.840
4911.78	26.0	3.928	−1.730
4917.23	26.0	4.191	−1.100
4918.01	26.0	4.230	−1.270
4927.42	26.0	3.573	−2.103

4930.31	26.0	3.960	−1.351
4938.81	26.0	2.875	−1.027
4939.24	26.0	4.154	−1.069
4939.69	26.0	0.859	−3.170
4946.39	26.0	3.368	−0.980
4950.11	26.0	3.417	−1.590
4961.91	26.0	3.634	−2.460
4962.57	26.0	4.178	−1.322
4966.09	26.0	3.332	−0.731
4969.92	26.0	4.217	−0.810
4973.10	26.0	3.960	−0.740
4982.50	26.0	4.103	−0.196
4983.25	26.0	4.154	−0.312
4983.85	26.0	4.103	−0.246
4985.25	26.0	3.928	−0.590
4985.55	26.0	2.865	−1.382
4985.98	26.0	4.256	−1.870
4999.11	26.0	4.186	−1.770
5002.79	26.0	3.396	−1.490
5005.71	26.0	3.884	−0.339
5006.70	26.0	2.588	−4.097
5014.94	26.0	3.943	−0.283
5022.24	26.0	3.984	−0.450
5031.91	26.0	4.371	−1.750
5040.25	26.0	4.220	−2.429
5074.75	26.0	4.220	−0.050
5078.98	26.0	4.301	−0.322
5079.22	26.0	2.198	−2.057
5083.34	26.0	0.958	−3.008

5088.15	26.0	4.154	−1.760
5090.77	26.0	4.256	−0.500
5126.19	26.0	4.256	−0.930
5127.36	26.0	0.915	−3.327
5127.68	26.0	0.052	−6.065
5137.38	26.0	4.178	−0.200
5141.74	26.0	2.424	−2.124
5145.09	26.0	2.198	−3.266
5162.27	26.0	4.178	0.090
5191.45	26.0	3.038	−0.551
5194.94	26.0	1.557	−2.150
5195.47	26.0	4.220	−0.156
5197.94	26.0	4.301	−1.580
5198.71	26.0	2.223	−2.195
5215.18	26.0	3.266	−0.801
5216.27	26.0	1.608	−2.170
5217.39	26.0	3.211	−1.000
5217.92	26.0	3.640	−2.139
5218.51	26.0	4.580	−2.620
5223.18	26.0	3.635	−2.353
5226.86	26.0	3.038	−0.755
5227.19	26.0	1.557	−1.408
5228.38	26.0	4.220	−1.160
5229.85	26.0	3.283	−1.507
5232.94	26.0	2.940	−0.028
5236.20	26.0	4.186	−1.737
5242.49	26.0	3.634	−1.057
5243.78	26.0	4.256	−1.110
5364.87	26.0	4.445	0.208

5365.40	26.0	3.573	−1.280
5367.47	26.0	4.415	0.263
5369.96	26.0	4.371	0.396
5373.71	26.0	4.473	−0.880
5379.57	26.0	3.694	−1.654
5383.37	26.0	4.312	0.485
5386.33	26.0	4.154	−1.820
5389.48	26.0	4.415	−0.400
5393.17	26.0	3.241	−0.605
5397.62	26.0	3.634	−2.500
5403.82	26.0	4.076	−1.214
5405.35	26.0	4.386	−1.350
5405.77	26.0	0.990	−1.984
5406.77	26.0	4.371	−1.520
5410.91	26.0	4.473	0.438
5415.20	26.0	4.386	0.512
5417.03	26.0	4.415	−1.500
5422.15	26.0	4.320	−2.250
5424.07	26.0	4.320	0.550
5432.95	26.0	4.445	−0.790
5434.52	26.0	1.011	−2.222
5436.30	26.0	4.386	−1.450
5445.04	26.0	4.386	0.050
5461.55	26.0	4.445	−1.710
5462.96	26.0	4.473	−0.315
5463.28	26.0	4.434	−0.050
5464.28	26.0	4.143	−1.702
5466.40	26.0	4.371	−0.670
5499.59	26.0	4.473	−2.730

5501.47	26.0	0.958	–2.937
5505.88	26.0	4.415	–2.668
5506.78	26.0	0.990	–2.857
5522.45	26.0	4.209	–1.540
5543.94	26.0	4.217	–1.150
5546.51	26.0	4.371	–1.190
5554.89	26.0	4.548	–0.370
5560.21	26.0	4.434	–1.150
5565.70	26.0	4.608	–0.293
5569.62	26.0	3.417	–0.406
5570.05	26.0	2.845	–4.277
5576.09	26.0	3.430	–0.730
5584.76	26.0	3.573	–2.450
5586.76	26.0	3.368	–0.120
5595.06	26.0	5.064	–1.700
5611.36	26.0	3.635	–3.030
5615.30	26.0	2.588	–2.528
5615.64	26.0	3.332	0.000
5618.63	26.0	4.209	–1.416
5619.60	26.0	4.386	–1.580
5624.02	26.0	4.386	–1.270
5624.54	26.0	3.417	–0.655
5627.08	26.0	4.178	–3.004
5635.82	26.0	4.256	–1.670
5636.70	26.0	3.640	–2.590
5638.26	26.0	4.220	–0.850
5641.43	26.0	4.256	–1.180
5649.99	26.0	5.099	–0.800
5650.71	26.0	5.085	–0.830

5652.32	26.0	4.260	–1.860
5653.86	26.0	4.386	–1.500
5655.18	26.0	5.064	–0.610
5661.02	26.0	4.580	–2.400
5661.35	26.0	4.284	–1.956
5662.52	26.0	4.178	–0.503
5678.38	26.0	3.883	–3.050
5678.60	26.0	2.424	–4.590
5679.02	26.0	4.652	–0.850
5680.24	26.0	4.186	–2.420
5698.02	26.0	3.640	–2.790
5701.54	26.0	2.559	–2.216
5705.46	26.0	4.301	–1.575
5724.45	26.0	4.284	–2.650
5731.76	26.0	4.256	–1.190
5752.03	26.0	4.549	–0.997
5753.12	26.0	4.260	–0.668
5760.34	26.0	3.642	–2.550
5775.08	26.0	4.220	–1.238
5778.45	26.0	2.588	–3.600
5778.81	26.0	4.559	–3.040
5791.52	26.0	4.584	–2.126
5793.68	26.0	4.593	–2.586
5793.91	26.0	4.220	–1.750
5806.72	26.0	4.607	–1.000
5809.22	26.0	3.883	–1.830
5811.91	26.0	4.143	–2.440
5814.81	26.0	4.283	–1.960
5816.06	26.0	4.294	–2.310

5816.37	26.0	4.548	–0.691
5838.37	26.0	3.943	–2.380
5844.92	26.0	4.154	–2.950
5848.13	26.0	4.608	–1.936
5855.08	26.0	4.608	–1.668
5856.09	26.0	4.294	–1.698
5858.78	26.0	4.220	–2.290
5859.59	26.0	4.549	–0.609
5862.36	26.0	4.549	–0.387
5881.75	26.0	2.176	–4.810
5883.82	26.0	3.960	–1.370
5905.67	26.0	4.652	–0.850
5909.97	26.0	3.211	–2.797
5927.79	26.0	4.652	–1.160
5929.68	26.0	4.548	–1.340
5930.18	26.0	4.652	–0.230
5956.69	26.0	0.859	–4.625
5983.68	26.0	4.549	–0.718
5987.06	26.0	4.796	–0.599
6003.01	26.0	3.881	–1.120
6005.54	26.0	2.588	–3.895
6007.96	26.0	4.652	–0.767
6008.56	26.0	3.884	–0.986
6015.24	26.0	2.223	–4.670
6024.06	26.0	4.548	–0.020
6027.05	26.0	4.076	–1.159
6056.00	26.0	4.733	–0.460
6065.48	26.0	2.608	–1.490
6078.49	26.0	4.796	–0.381

6079.01	26.0	4.652	−1.120
6093.64	26.0	4.607	−1.450
6094.37	26.0	4.652	−1.690
6096.66	26.0	3.984	−1.980
6102.17	26.0	4.835	−0.266
6120.25	26.0	0.915	−5.960
6136.61	26.0	2.453	−1.400
6136.99	26.0	2.198	−3.000
6137.69	26.0	2.588	−1.353
6151.62	26.0	2.176	−3.409
6157.73	26.0	4.076	−1.280
6165.36	26.0	4.143	−1.634
6173.33	26.0	2.223	−2.980
6180.20	26.0	2.727	−2.806
6187.40	26.0	2.832	−4.218
6187.99	26.0	3.943	−1.840
6191.56	26.0	2.433	−1.487
6200.31	26.0	2.608	−2.457
6213.43	26.0	2.223	−2.612
6215.14	26.0	4.186	−1.441
6219.28	26.0	2.198	−2.423
6229.23	26.0	2.845	−3.025
6230.72	26.0	2.559	−1.241
6232.64	26.0	3.654	−1.333
6240.65	26.0	2.223	−3.413
6246.32	26.0	3.602	−0.703
6335.33	26.0	2.198	−2.207
6336.82	26.0	3.686	−0.686
6355.03	26.0	2.845	−2.380

6358.70	26.0	0.859	–4.418
6393.60	26.0	2.433	–1.572
6419.95	26.0	4.733	–0.270
6421.35	26.0	2.279	–2.017
6436.41	26.0	4.186	–2.510
6481.87	26.0	2.279	–3.014
6483.94	26.0	1.485	–5.398
6518.37	26.0	2.831	–2.670
6546.24	26.0	2.758	–1.806
6574.23	26.0	0.990	–5.003
6575.02	26.0	2.588	–2.800
6581.21	26.0	1.485	–4.829
6592.91	26.0	2.727	–1.603
6593.87	26.0	2.433	–2.342
6597.56	26.0	4.795	–1.070
6609.11	26.0	2.559	–2.672
6703.57	26.0	2.758	–3.130
6726.67	26.0	4.607	–1.123
6739.52	26.0	1.557	–4.984
6745.10	26.0	4.580	–2.170
6746.95	26.0	2.608	–4.350
6750.15	26.0	2.424	–2.481
6806.84	26.0	2.727	–3.240
6810.26	26.0	4.607	–1.126
6839.83	26.0	2.559	–3.470
6841.34	26.0	4.607	–0.790
6842.69	26.0	4.638	–1.280
6843.65	26.0	4.548	–0.980
6844.67	26.0	1.557	–5.507

6933.62	26.0	2.43	–3.598
6936.48	26.0	4.61	–2.280
6945.20	26.0	2.42	–2.452
6951.25	26.0	4.56	–1.061
6951.62	26.0	4.28	–2.562
6971.93	26.0	3.02	–3.480
6999.88	26.0	4.10	–1.510
7000.61	26.0	4.14	–2.126
7007.97	26.0	4.18	–1.870
7038.22	26.0	4.22	–1.150
7071.86	26.0	4.61	–1.600
7083.40	26.0	4.91	–1.382
7086.73	26.0	3.60	–2.677
7090.38	26.0	4.23	–1.090
7091.92	26.0	4.96	–1.478
7112.17	26.0	2.99	–3.008
7114.55	26.0	2.69	–4.080
7151.47	26.0	2.48	–3.600
7179.99	26.0	1.49	–4.770
7212.44	26.0	4.96	–1.102
7219.68	26.0	4.08	–1.680
4416.83	26.1	2.778	–2.600
4491.40	26.1	2.856	–2.640
4520.22	26.1	2.807	–2.620
4555.89	26.1	2.828	–2.250
4656.98	26.1	2.891	–3.570
4731.45	26.1	2.891	–3.130
4825.74	26.1	2.635	–5.012
4833.20	26.1	2.657	–4.785

4923.93	26.1	2.891	−1.206
4993.36	26.1	2.807	−3.680
5197.58	26.1	3.230	−2.054
5234.63	26.1	3.221	−2.219
5414.07	26.1	3.221	−3.482
5425.26	26.1	3.199	−3.390
5991.38	26.1	3.153	−3.657
6084.11	26.1	3.199	−3.881
6149.26	26.1	3.889	−2.841
6238.39	26.1	3.889	−2.754
6247.56	26.1	3.892	−2.435
6432.68	26.1	2.891	−3.507

Appendix B

Other element line list

Table B.1: Linelist for the other elements.

Wavelength	Element and I.S.	E.P.	$\log(gf)$
6696.02	13.0	3.14	-1.57
7835.31	13.0	4.02	-0.65
7836.13	13.0	4.02	-0.49
5690.43	14.0	4.93	-1.79
5772.14	14.0	5.08	-1.62
5793.09	14.0	4.93	-1.91
5948.55	14.0	5.08	-1.11
6142.49	14.0	5.62	-1.48
6145.02	14.0	5.61	-1.40
6155.15	14.0	5.62	-0.75
6721.86	14.0	5.86	-1.09
5261.70	20.0	2.52	-0.59
5512.98	20.0	2.93	-0.71
5588.75	20.0	2.53	+0.31
5590.14	20.0	2.52	-0.59

5601.27	20.0	2.53	-0.55
6102.72	20.0	1.88	-0.79
6122.22	20.0	1.89	-0.32
6161.29	20.0	2.52	-1.29
6162.17	20.0	1.90	-0.09
6166.44	20.0	2.52	-1.16
6169.04	20.0	2.52	-0.80
6169.56	20.0	2.53	-0.53
6439.08	20.0	2.53	+0.39
6455.59	20.0	2.52	-1.56
6493.78	20.0	2.52	+0.02
6499.65	20.0	2.52	-0.72
6717.68	20.0	2.71	-0.59
4981.73	22.0	0.85	+0.50
4997.09	22.0	0.00	-2.12
4999.50	22.0	0.83	+0.25
5009.64	22.0	0.02	-2.26
5016.16	22.0	0.85	-0.57
5020.02	22.0	0.84	-0.42
5022.87	22.0	0.83	-0.43
5043.58	22.0	0.84	-1.73
5045.41	22.0	0.85	-1.99
5145.46	22.0	1.46	-0.57
5147.47	22.0	0.00	-2.01
5210.38	22.0	0.05	-0.88
5219.70	22.0	0.02	-2.29
5426.23	22.0	0.02	-3.01
5460.46	22.0	0.05	-2.80
5953.16	22.0	1.89	-0.33

6064.62	22.0	1.05	-1.94
6258.10	22.0	1.44	-0.36
6258.70	22.0	1.46	-0.24
6261.10	22.0	1.43	-0.48
5005.15	22.1	1.57	-2.54
5013.67	22.1	1.58	-1.99
5185.91	22.1	1.89	-1.35
5336.77	22.1	1.58	-1.70
5381.01	22.1	1.57	-2.08
5396.22	22.1	1.58	-3.02
5418.75	22.1	1.58	-2.11
6491.56	22.1	2.06	-1.79
5225.81	24.0	2.71	-1.50
5247.57	24.0	0.96	-1.59
5345.80	24.0	1.00	-0.95
5348.31	24.0	1.00	-1.21
5409.77	24.0	1.03	-0.67
5035.36	28.0	3.64	+0.29
5080.53	28.0	3.66	+0.13
5084.09	28.0	3.68	+0.03
5146.48	28.0	3.71	-0.06
5578.71	28.0	1.68	-2.64
6586.31	28.0	1.95	-2.81
6767.77	28.0	1.83	-2.17
5087.42	39.1	1.08	-0.17
5119.11	39.1	0.99	-1.36
5200.41	39.1	0.99	-0.57
5205.73	39.1	1.03	-0.34
5289.82	39.1	1.03	-1.85

5112.28	40.1	1.66	-0.59
5309.27	44.0	0.93	-1.39
5699.06	44.0	1.09	-1.47
5274.23	58.1	1.04	+0.13
5330.56	58.1	0.87	-0.40
5092.79	60.1	0.38	-0.61
5132.33	60.1	0.56	-0.71
5212.36	60.1	0.20	-0.96
5249.58	60.1	0.98	+0.20
5319.81	60.1	0.55	-0.14
5485.70	60.1	1.26	-0.12
5804.00	60.1	0.74	-0.53
6170.06	68.1	0.06	-2.77

References

A. Alonso, S. Arribas, and C. Martínez-Roger. The effective temperature scale of giant stars (F0-K5). II. Empirical calibration of T$_{eff}$ versus colours and [Fe/H]. *A&AS*, 140:261–277, December 1999.

A. Arellano Ferro, D. M. Bramich, S. Giridhar, R. Figuera Jaimes, N. Kains, and K. Kuppuswamy. Variable Stars in the Globular Cluster NGC 288: [Fe/H] and Distance. *Acta Astron.*, 63:429–451, December 2013.

K. M. Ashman and S. E. Zepf. Globular cluster systems. *Cambridge Astrophysics Series*, 30, 1998.

S. I. Bailey. A discussion of variable stars in the cluster ω Centauri. *Annals of Harvard College Observatory*, 38:1, 1902.

E. E. Barnard. Some abnormal stars in the cluster M13 in Hercules. *ApJ*, 12:176–181, October 1900.

S. A. Barnes. Search for Variables in the Globular Cluster NGC 7492. *AJ*, 73:579, September 1968.

C. Bartolini, F. Grilli, and F. Morisi. Observations of Variable Stars in NGC 1261. *Information Bulletin on Variable Stars*, 662:1, April 1972.

L. R. Bedin, G. Piotto, J. Anderson, S. Cassisi, I. R. King, Y. Momany, and G. Carraro. ω Centauri: The Population Puzzle Goes Deeper. *ApJL*, 605:L125–L128, April 2004.

T. C. Beers and N. Christlieb. The Discovery and Analysis of Very Metal-Poor Stars in the Galaxy. *ARA&A*, 43:531–580, September 2005.

R. A. Bell, R. J. Dickens, and B. Gustafsson. Carbon abundances in red giant stars in the globular clusters M92 and NGC 6397. *ApJ*, 229:604–623, April 1979.

M. Bellazzini. Dwarf Galaxies and Globular Clusters. *Highlights of Astronomy*, 16: 271–272, March 2015.

M. Benacquista. Relativistic Binaries in Globular Clusters. *Living Reviews in Relativity*, 5:2, February 2002.

R. Bernstein, S. A. Shectman, S. M. Gunnels, S. Mochnacki, and A. E. Athey. MIKE: A Double Echelle Spectrograph for the Magellan Telescopes at Las Campanas Observatory. In M. Iye and A. F. M. Moorwood, editors, *Instrument Design and Performance for Optical/Infrared Ground-based Telescopes*, volume 4841 of *Society of Photo-Optical Instrumentation Engineers (SPIE) Conference Series*, pages 1694–1704, March 2003.

H. A. Bethe. Energy Production in Stars. *Physical Review*, 55:434–456, March 1939.

A. I. Boothroyd and I.-J. Sackmann. The CNO Isotopes: Deep Circulation in Red Giants and First and Second Dredge-up. *ApJ*, 510:232–250, January 1999.

G. H. Bowen. Dynamical modeling of long-period variable star atmospheres. *ApJ*, 329:299–317, June 1988.

V. Bromm and R. B. Larson. The First Stars. *ARA&A*, 42:79–118, September 2004.

E. M. Burbidge, G. R. Burbidge, W. A. Fowler, and F. Hoyle. Synthesis of the Elements in Stars. *Reviews of Modern Physics*, 29:547–650, 1957.

M. Busso, R. Gallino, and G. J. Wasserburg. Nucleosynthesis in Asymptotic Giant Branch Stars: Relevance for Galactic Enrichment and Solar System Formation. *ARA&A*, 37:239–309, 1999.

V. Caloi and F. D'Antona. Helium self-enrichment in globular clusters and the second parameter problem in M 3 and M 13. *A&A*, 435:987–993, June 2005.

A. G. W. Cameron. Nuclear Reactions in Stars and Nucleogenesis. *PASP*, 69:201, June 1957.

S. W. Campbell, V. D'Orazi, D. Yong, T. N. Constantino, J. C. Lattanzio, R. J. Stancliffe, G. C. Angelou, E. C. Wylie-de Boer, and F. Grundahl. Sodium content as a predictor of the advanced evolution of globular cluster stars. *Nature*, 498:198–200, June 2013.

E. Carretta, A. Bragaglia, R. Gratton, and S. Lucatello. Na-O anticorrelation and HB. VIII. Proton-capture elements and metallicities in 17 globular clusters from UVES spectra. *A&A*, 505:139–155, October 2009a.

E. Carretta, A. Bragaglia, R. G. Gratton, S. Lucatello, G. Catanzaro, F. Leone, M. Bellazzini, R. Claudi, V. D'Orazi, Y. Momany, S. Ortolani, E. Pancino, G. Piotto, A. Recio-Blanco, and E. Sabbi. Na-O anticorrelation and HB. VII. The chemical

composition of first and second-generation stars in 15 globular clusters from GI-RAFFE spectra. *A&A*, 505:117–138, October 2009b.

E. Carretta, A. Bragaglia, R. G. Gratton, S. Lucatello, and V. D'Orazi. Chemical Tagging of Three Distinct Populations of Red Giants in the Globular Cluster NGC 6752. *ApJL*, 750:L14, May 2012.

B. W. Carroll and D. A. Ostlie. *An Introduction to Modern Astrophysics*. 1996.

M. Catelan. The ages of stars: The horizontal branch. In E. E. Mamajek, D. R. Soderblom, and R. F. G. Wyse, editors, *IAU Symposium*, volume 258 of *IAU Symposium*, pages 209–220, June 2009.

W. Chantereau, C. Charbonnel, and T. Decressin. Evolution of long-lived globular cluster stars I. Grid of stellar models with helium enhancement at [Fe/H] = -1.75. *ArXiv e-prints*, April 2015.

C. Charbonnel. Clues for non-standard mixing on the red giant branch from C-12/C-13 and C-12/N-14 ratios in evolved stars. *A&A*, 282:811–820, February 1994.

C. M. Clement. An Update to the Web Edition of the Catalogue of Variable Stars in Galactic Globular Clusters. In C. Sterken, N. Samus, and L. Szabados, editors, *Variable Stars, the Galactic halo and Galaxy Formation*, page 23, February 2010.

M. Cuntz and D. G. Luttermoser. Stochastic shock waves as a candidate mechanism for the formation of the He I 10830-A line in cool giant stars. *ApJL*, 353:L39–L43, April 1990.

T. Decressin, C. Charbonnel, and G. Meynet. Origin of the abundance patterns in Galactic globular clusters: constraints on dynamical and chemical properties of globular clusters. *A&A*, 475:859–873, December 2007.

P. A. Denissenkov and F. Herwig. The Abundance Evolution of Oxygen, Sodium, and Magnesium in Extremely Metal Poor Intermediate-Mass Stars: Implications for the Self-Pollution Scenario in Globular Clusters. *ApJL*, 590:L99–L102, June 2003.

R. G. Deupree and R. K. Wallace. The core helium flash and surface abundance anomalies. *ApJ*, 317:724–732, June 1987.

V. D'Orazi, M. Lugaro, S. W. Campbell, A. Bragaglia, E. Carretta, R. G. Gratton, S. Lucatello, and F. D'Antona. Rubidium Abundances in the Globular Clusters NGC 6752, NGC 1904, and NGC 104 (47 Tuc). *ApJ*, 776:59, October 2013.

A. Dotter, B. Chaboyer, D. Jevremović, E. Baron, J. W. Ferguson, A. Sarajedini, and J. Anderson. The ACS Survey of Galactic Globular Clusters. II. Stellar Evolution

Tracks, Isochrones, Luminosity Functions, and Synthetic Horizontal-Branch Models. *AJ*, 134:376–390, July 2007.

A. K. Dupree, L. Hartmann, and E. H. Avrett. Chromospheres and mass loss in metal-deficient giant stars. *ApJL*, 281:L37–L39, June 1984.

M. Elitzur, Ž. Ivezić, and D. Vinković. The structure of winds in AGB stars. In Y. Nakada, M. Honma, and M. Seki, editors, *Mass-Losing Pulsating Stars and their Circumstellar Matter*, volume 283 of *Astrophysics and Space Science Library*, pages 265–273, April 2003.

J. Faulkner. On the Nature of the Horizontal Branch. I. *ApJ*, 144:978, June 1966.

R. Figuera Jaimes, A. Arellano Ferro, D. M. Bramich, S. Giridhar, and K. Kuppuswamy. Variable stars in the globular cluster NGC 7492. New discoveries and physical parameter determination. *A&A*, 556:A20, August 2013.

A. Frebel. Stellar archaeology: Exploring the Universe with metal-poor stars. *Astronomische Nachrichten*, 331:474–488, May 2010a.

A. Frebel. Stellar Archaeology: New Science with Old Stars. *ArXiv e-prints*, December 2010b.

A. Frebel, W. Aoki, N. Christlieb, H. Ando, M. Asplund, P. S. Barklem, T. C. Beers, K. Eriksson, C. Fechner, M. Y. Fujimoto, S. Honda, T. Kajino, T. Minezaki, K. Nomoto, J. E. Norris, S. G. Ryan, M. Takada-Hidai, S. Tsangarides, and Y. Yoshii. Nucleosynthetic signatures of the first stars. *Nature*, 434:871–873, April 2005.

D. A. García-Hernández, O. Zamora, A. Yagüe, S. Uttenthaler, A. I. Karakas, M. Lugaro, P. Ventura, and D. L. Lambert. Hot bottom burning and s-process nucleosynthesis in massive AGB stars at the beginning of the thermally-pulsing phase. *A&A*, 555:L3, July 2013.

D. Geisler. Abundance determinations for three galactic globular clusters. *PASP*, 100:687–692, June 1988.

O. Y. Gnedin. Formation of Globular Clusters: In and Out of Dwarf Galaxies. In M. Kissler-Patig, editor, *Extragalactic Globular Cluster Systems*, page 224, 2003.

R. G. Gratton, E. Carretta, A. Bragaglia, S. Lucatello, and V. D'Orazi. The second and third parameters of the horizontal branch in globular clusters. *A&A*, 517:A81, July 2010a.

R. G. Gratton, V. D'Orazi, A. Bragaglia, E. Carretta, and S. Lucatello. The connec-

tion between missing AGB stars and extended horizontal branches. *A&A*, 522:A77, November 2010b.

R. G. Gratton, C. Sneden, E. Carretta, and A. Bragaglia. Mixing along the red giant branch in metal-poor field stars. *A&A*, 354:169–187, February 2000.

B. Gustafsson, R. A. Bell, K. Eriksson, and A. Nordlund. A grid of model atmospheres for metal-deficient giant stars. I. *A&A*, 42:407–432, September 1975.

H. J. Habing. Circumstellar envelopes and Asymptotic Giant Branch stars. *A&A Rev.*, 7:97–207, 1996.

W. E. Harris. A Catalog of Parameters for Globular Clusters in the Milky Way. *AJ*, 112:1487, October 1996.

F. Herwig. Evolution of Asymptotic Giant Branch Stars. *ARA&A*, 43:435–479, September 2005.

G. Hinshaw, J. L. Weiland, R. S. Hill, N. Odegard, D. Larson, C. L. Bennett, J. Dunkley, B. Gold, M. R. Greason, N. Jarosik, E. Komatsu, M. R. Nolta, L. Page, D. N. Spergel, E. Wollack, M. Halpern, A. Kogut, M. Limon, S. S. Meyer, G. S. Tucker, and E. L. Wright. Five-Year Wilkinson Microwave Anisotropy Probe Observations: Data Processing, Sky Maps, and Basic Results. *ApJS*, 180:225–245, February 2009.

S. Honda, W. Aoki, N. Arimoto, K. Sadakane, K. Otsuki, T. Kajino, and G. J. Mathews. Heavy elements in globular clusters and dwarf galaxies as probes of the origin of r-process elements. In S. Kubono, T. Hayakawa, T. Kajino, H. Miyatake, T. Motobayashi, and K. Nomoto, editors, *American Institute of Physics Conference Series*, volume 1484 of *American Institute of Physics Conference Series*, pages 99–104, November 2012.

F. Hoyle and M. Schwarzschild. On the Evolution of Type II Stars. *ApJS*, 2:1, June 1955.

I. Iben and A. Renzini. Single star evolution I. Massive stars and early evolution of low and intermediate mass stars. *Phys. Rep.*, 105:329–406, March 1984.

I. Iben, Jr. The Surface Ration of N^{14} to C^{12} during Helium Burning. *ApJ*, 140:1631, November 1964.

I. Iben, Jr. Stellar Evolution Within and off the Main Sequence. *ARA&A*, 5:571, 1967.

I. Iben, Jr. and A. Renzini. Asymptotic giant branch evolution and beyond. *ARA&A*, 21:271–342, 1983.

G. H. Jacoby, O. De Marco, J. E. Davies, J. P. Harrington, and H. E. Bond. Are

REFERENCES

Planetary Nebulae in Globular Clusters a Binary Phenomenon? In *American Astronomical Society Meeting Abstracts #223*, volume 223 of *American Astronomical Society Meeting Abstracts*, page 353.25, January 2014.

G. James, P. François, P. Bonifacio, E. Carretta, R. G. Gratton, and F. Spite. Heavy elements and chemical enrichment in globular clusters. *A&A*, 427:825–838, December 2004.

R. Jimenez. Globular Cluster Ages. *Proceedings of the National Academy of Science*, 95:13–17, January 1998.

C. I. Johnson, I. McDonald, C. A. Pilachowski, M. Mateo, J. I. Bailey, III, M. J. Cordero, A. A. Zijlstra, J. D. Crane, E. Olszewski, S. A. Shectman, and I. Thompson. AGB Sodium Abundances in the Globular Cluster 47 Tucanae (NGC 104). *AJ*, 149:71, February 2015.

C. I. Johnson, A. McWilliam, and R. M. Rich. Chemical Abundance Analysis of a Neutron-capture Enhanced Red Giant in the Bulge Plaut Field. *ApJL*, 775:L27, September 2013a.

C. I. Johnson and C. A. Pilachowski. Chemical Abundances for 855 Giants in the Globular Cluster Omega Centauri (NGC 5139). *ApJ*, 722:1373–1410, October 2010a.

C. I. Johnson and C. A. Pilachowski. Spectroscopic Abundances of Nearly All Bright Red Giants in Omega Centauri. In *American Astronomical Society Meeting Abstracts #215*, volume 42 of *Bulletin of the American Astronomical Society*, page 455.08, January 2010b.

C. I. Johnson and C. A. Pilachowski. Oxygen and Sodium Abundances in M13 (NGC 6205) Giants: Linking Globular Cluster Formation Scenarios, Deep Mixing, and Post-RGB Evolution. *ApJL*, 754:L38, August 2012.

C. I. Johnson, C. A. Pilachowski, J. Simmerer, and D. Schwenk. Fe and Al Abundances for 180 Red Giants in the Globular Cluster Omega Centauri (NGC 5139). *ApJ*, 681: 1505–1523, July 2008.

C. I. Johnson, R. M. Rich, C. Kobayashi, and J. P. Fulbright. Constraints on the Formation of the Galactic Bulge from Na, Al, and Heavy-element Abundances in Plaut's Field. *ApJ*, 749:175, April 2012.

C. I. Johnson, R. M. Rich, C. Kobayashi, A. Kunder, and A. Koch. Light, Alpha, and Fe-peak Element Abundances in the Galactic Bulge. *AJ*, 148:67, October 2014a.

C. I. Johnson, R. M. Rich, A. Kunder, and C. A. Pilachowski. Chemical Abundance

Patterns of Galactic Bulge Globular Clusters. In *American Astronomical Society Meeting Abstracts #223*, volume 223 of *American Astronomical Society Meeting Abstracts*, page 442.22, January 2014b.

C. I. Johnson, R. M. Rich, C. A. Pilachowski, and A. M. Kunder. Chemical Abundances of Red Giant Branch Stars in the Globular Clusters NGC 6333 and NGC 6366. In *American Astronomical Society Meeting Abstracts #221*, volume 221 of *American Astronomical Society Meeting Abstracts*, page 250.19, January 2013b.

S. Jones, R. Hirschi, K. Nomoto, T. Fischer, F. X. Timmes, F. Herwig, B. Paxton, H. Toki, T. Suzuki, G. Martínez-Pinedo, Y. H. Lam, and M. G. Bertolli. Advanced Burning Stages and Fate of 8-10 M$_{\rm L}$ Stars. *ApJ*, 772:150, August 2013.

N. Kains, D. M. Bramich, R. Figuera Jaimes, A. Arellano Ferro, S. Giridhar, and K. Kuppuswamy. Constraining the parameters of globular cluster NGC 1904 from its variable star population. *A&A*, 548:A92, December 2012.

D. Kamath, P. R. Wood, and H. Van Winckel. Optically Visible Post-AGB Stars, Post-RGB Stars and Young Stellar Objects in the Large Magellanic Cloud. *ArXiv e-prints*, August 2015.

R. Kurucz. ATLAS9 Stellar Atmosphere Programs and 2 km/s grid. *ATLAS9 Stellar Atmosphere Programs and 2 km/s grid. Kurucz CD-ROM No. 13. Cambridge, Mass.: Smithsonian Astrophysical Observatory, 1993.*, 13, 1993.

R. L. Kurucz. Model Atmospheres for Globular Cluster Stars. In A. G. D. Philip and D. S. Hayes, editors, *IAU Colloq. 68: Astrophysical Parameters for Globular Clusters*, page 289, 1981.

E. Lapenna, A. Mucciarelli, B. Lanzoni, F. R. Ferraro, E. Dalessandro, L. Origlia, and D. Massari. Non-local Thermodynamical Equilibrium Effects on the Iron Abundance of Asymptotic Giant Branch Stars in 47 Tucanae. *ApJ*, 797:124, December 2014.

J.-W. Lee. Variations in the Na-O anticorrelation in globular clusters: evidence for a deep mixing episode in red giant branch stars. *MNRAS*, 405:L36–L40, June 2010.

J.-W. Lee and B. W. Carney. BV Photometry of RR Lyrae Variables in the Globular Cluster M2 (NGC 7089). *AJ*, 117:2868–2881, June 1999.

K. Lodders. Solar System Abundances of the Elements. In A. Goswami and B. E. Reddy, editors, *Principles and Perspectives in Cosmochemistry*, page 379, 2010.

I. McDonald, M. L. Boyer, J. T. van Loon, A. A. Zijlstra, J. L. Hora, B. Babler,

M. Block, K. Gordon, M. Meade, M. Meixner, K. Misselt, T. Robitaille, M. Sewiło, B. Shiao, and B. Whitney. Fundamental Parameters, Integrated Red Giant Branch Mass Loss, and Dust Production in the Galactic Globular Cluster 47 Tucanae. *ApJS*, 193:23, April 2011.

I. McDonald and J. T. van Loon. Dust, pulsation, chromospheres and their rôle in driving mass loss from red giants in Galactic globular clusters. *A&A*, 476:1261–1282, December 2007.

I. McDonald, J. T. van Loon, L. Decin, M. L. Boyer, A. K. Dupree, A. Evans, R. D. Gehrz, and C. E. Woodward. Giants in the globular cluster ω Centauri: dust production, mass-loss and distance. *MNRAS*, 394:831–856, April 2009.

I. McDonald, J. T. van Loon, A. K. Dupree, and M. L. Boyer. Discovery of long-period variable stars in the very metal-poor globular cluster M15. *MNRAS*, 405:1711–1722, July 2010.

I. McDonald and A. A. Zijlstra. Globular cluster interstellar media: ionized and ejected by white dwarfs. *MNRAS*, 446:2226–2242, January 2015a.

I. McDonald and A. A. Zijlstra. Mass-loss on the red giant branch: the value and metallicity dependence of Reimers' η in globular clusters. *MNRAS*, 448:502–521, March 2015b.

I. McDonald, A. A. Zijlstra, and M. L. Boyer. Fundamental parameters and infrared excesses of Hipparcos stars. *MNRAS*, 427:343–357, November 2012.

A. P. Milone. Helium and multiple populations in the massive globular cluster NGC 6266 (M 62). *MNRAS*, 446:1672–1684, January 2015.

A. P. Milone, A. F. Marino, A. Dotter, J. E. Norris, H. Jerjen, G. Piotto, S. Cassisi, L. R. Bedin, A. Recio Blanco, A. Sarajedini, M. Asplund, M. Monelli, and A. Aparicio. Global and Nonglobal Parameters of Horizontal-branch Morphology of Globular Clusters. *ApJ*, 785:21, April 2014.

D. R. Mosley and R. E. White. Photometric Variability of Certain Red Giant Stars in the Globular Cluster NGC 7078 (M 15). In *Bulletin of the American Astronomical Society*, volume 7 of *Bulletin of the American Astronomical Society*, page 535, September 1975.

P. Murdin, editor. *Emission Spectrum*, page 4952. November 2000.

J. Norris, P. L. Cottrell, K. C. Freeman, and G. S. Da Costa. The abundance spread in the giants of NGC 6752. *ApJ*, 244:205–220, February 1981.

P. T. Oosterhoff. A semi-regular variable in NGC 288. *Bull. Astron. Inst. Netherlands*, 9:397, March 1943.

G. Piotto, S. Villanova, L. R. Bedin, R. Gratton, S. Cassisi, Y. Momany, A. Recio-Blanco, S. Lucatello, J. Anderson, I. R. King, A. Pietrinferni, and G. Carraro. Metallicities on the Double Main Sequence of ω Centauri Imply Large Helium Enhancement. *ApJ*, 621:777–784, March 2005.

O. R. Pols, C. A. Tout, J. C. Lattanzio, and A. I. Karakas. Thermal Pulses and Dredge-up in AGB Stars. In P. Podsiadlowski, S. Rappaport, A. R. King, F. D'Antona, and L. Burderi, editors, *Evolution of Binary and Multiple Star Systems*, volume 229 of *Astronomical Society of the Pacific Conference Series*, page 31, 2001.

J. C. Roediger, S. Courteau, G. Graves, and R. P. Schiavon. Constraining Stellar Population Models. I. Age, Metallicity and Abundance Pattern Compilation for Galactic Globular Clusters. *ApJS*, 210:10, January 2014.

L. Rosino. Ricerche sugli ammassi globulari. VIII - Stelle variabili e distanza dell' ammasso globulare NGC 1904 = M 79. *Mem. Soc. Astron. Italiana*, 23:101, 1952.

A. Sandage and G. Wallerstein. Color-Magnitude Diagram for Disk Clobular Cluster NGC 6356 Compared with Halo Clusters. *ApJ*, 131:598, May 1960.

A. Sandage and R. Wildey. The Anomalous Color-Magnitude Diagram of the Remote Globular Cluster NGC 7006. *ApJ*, 150:469, November 1967.

H. Sawyer Hogg. A third catalogue of variable stars in globular clusters comprising 2119 entries. *Publications of the David Dunlap Observatory*, 3:6, 1973.

R. Schneider, R. Valiante, P. Ventura, F. dell'Agli, M. Di Criscienzo, H. Hirashita, and F. Kemper. Dust production rate of asymptotic giant branch stars in the Magellanic Clouds. *MNRAS*, 442:1440–1450, August 2014.

K.-P. Schröder and M. Cuntz. A New Version of Reimers' Law of Mass Loss Based on a Physical Approach. *ApJL*, 630:L73–L76, September 2005.

H. Shapley. No. 107. Note on the densities of second-type stars. *Contributions from the Mount Wilson Observatory / Carnegie Institution of Washington*, 107:1–12, 1915.

M. D. Shetrone. MG and AL Abundances in Halo Globular Clusters. In H. L. Morrison and A. Sarajedini, editors, *Formation of the Galactic Halo...Inside and Out*, volume 92 of *Astronomical Society of the Pacific Conference Series*, page 383, April 1996.

M. D. Shetrone and M. J. Keane. Spectral Comparison of Red Giants in the Second-

Parameter Globular Cluster Pair NGC 288 and NGC 362. *AJ*, 119:840–850, February 2000.

L. J. Shingles, A. I. Karakas, R. Hirschi, C. K. Fishlock, D. Yong, G. S. Da Costa, and A. F. Marino. The s-Process Enrichment of the Globular Clusters M4 and M22. *ApJ*, 795:34, November 2014.

L. Siess. Evolution of massive AGB stars. III. the thermally pulsing super-AGB phase. *A&A*, 512:A10, March 2010.

V. V. Smith, M. D. Shetrone, and M. J. Keane. Lithium in a Cool Red Giant Member of the Globular Cluster NGC 362. *ApJL*, 516:L73–L76, May 1999.

C. Sneden. The nitrogen abundance of the very metal-poor star HD 122563. *ApJ*, 184: 839–849, September 1973.

C. Sneden, J. J. Cowan, and R. Gallino. Constraints on the Nature of the s- and r-processes. In K. Cunha, M. Spite, and B. Barbuy, editors, *IAU Symposium*, volume 265 of *IAU Symposium*, pages 46–53, March 2010.

C. Sneden, C. A. Pilachowski, and R. P. Kraft. Barium and Sodium Abundances in the Globular Clusters M15 and M92. *AJ*, 120:1351–1363, September 2000.

R. J. Stancliffe, R. G. Izzard, and C. A. Tout. Third dredge-up in low-mass stars: solving the Large Magellanic Cloud carbon star mystery. *MNRAS*, 356:L1–L5, January 2005.

N. B. Suntzeff. Carbon and nitrogen abundances in the giant stars of the globular clusters M3 and M13. *ApJS*, 47:1–32, September 1981.

P. ten Bruggencate. *Sternhaufen: Ihr Bau, Ihre Stellung zum Sternsystem und Ihre Bedeutung für die Kosmogonie*. January 1927.

S. van den Bergh. UBV photometry of globular clusters. *AJ*, 72:70–81, February 1967.

H. van Winckel. Post-AGB Stars. *ARA&A*, 41:391–427, 2003.

D. A. Vandenberg and G. H. Smith. Constraints from stellar models on mixing as a viable explanation of abundance anomalies in globular clusters. *PASP*, 100:314–335, March 1988.

P. Ventura, F. D'Antona, I. Mazzitelli, and R. Gratton. Predictions for Self-Pollution in Globular Cluster Stars. *ApJL*, 550:L65–L69, March 2001.

S. Villanova, G. Piotto, I. R. King, J. Anderson, L. R. Bedin, R. G. Gratton, S. Cassisi, Y. Momany, A. Bellini, A. M. Cool, A. Recio-Blanco, and A. Renzini. The

Multiplicity of the Subgiant Branch of ω Centauri: Evidence for Prolonged Star Formation. *ApJ*, 663:296–314, July 2007.

A. Wehlau and S. Demers. NGC 1261 and the Oosterhoff type I systems. *A&A*, 57: 251–256, May 1977.

D. E. Welty. A search for giant and asymptotic-giant-branch variable stars in six globular clusters. *AJ*, 90:2555–2574, December 1985.

J. M. Winters, T. Le Bertre, K. S. Jeong, C. Helling, and E. Sedlmayr. A systematic investigation of the mass loss mechanism in dust forming long-period variable stars. *A&A*, 361:641–659, September 2000.

P. R. Wood. Pulsation and mass loss in Mira variables. *ApJ*, 227:220–231, January 1979.

C. C. Worley, V. Hill, J. Sobeck, and E. Carretta. Ba and Eu abundances in M 15 giant stars. *A&A*, 553:A47, May 2013.

D. Yong, A. I. Karakas, D. L. Lambert, A. Chieffi, and M. Limongi. Insights into the s-process and r-process as revealed by globular clusters. In K. Cunha, M. Spite, and B. Barbuy, editors, *IAU Symposium*, volume 265 of *IAU Symposium*, pages 54–56, March 2010.